FY20 National Laser Users' Facility Program

M. S. Wei

Laboratory for Laser Energetics, University of Rochester

During FY19, the National Nuclear Security Administration (NNSA) and Office of Science jointly completed a funding opportunity announcement (FOA), review, and selection process for National Laser Users' Facility (NLUF) experiments to be conducted at the Omega Facility during FY20 and FY21. After peer review by an independent proposal review committee for scientific and technical merit and the feasibility review by the Omega Facility team, NNSA selected 11 proposals for funding and Omega shot allocation with a total of 22.5 and 23.5 shot days for experiments in FY20 and FY21, respectively. During the first half of the FY20, LLE completed a one-time solicitation, review, and selection process for Academic and Industrial Basic Science (AIBS) experiments to utilize the remaining NLUF shot allocation in FY20–FY21. Ten new projects were selected for AIBS shot allocation (a total of 11 and 10 shot days) for experiments staring in Q3FY20 and throughout FY21.

FY20 was the first of a two-year period of performance for these 21 NLUF including AIBS projects (Table I). Fifteen NLUF and AIBS projects obtained a total of 232 target shots during FY20, which are summarized in this section.

A critical part of the NNSA-supported NLUF program and the DOE Office of Fusion Energy Sciences (FES)-supported LaserNetUS program is the education and training of graduate students in high-energy-density (HED) physics. In addition, graduate students can also access the Omega Laser Facility to conduct their theses research through collaborations with national laboratories and LLE. In total, about 60 graduate students from 18 universities participated in these external user-led research projects supported by NLUF/Laser Basic Science (LBS), LaserNetUS, and/or with experiments conducted at the Omega Laser Facility (see Table II), among which nine students successfully defended their Ph.D. theses in calendar year 2020 (see the highlighted names in Table II). It is worth noting that 18 of these students are new to the Omega Laser Facility.

Measurements of Ion–Electron Equilibration Utilizing Low-Velocity Ion Stopping in High-Energy-Density Plasmas on OMEGA

Principal Investigators: P. J. Adrian, J. A. Frenje, N. Kabadi, M. Gatu Johnson, A. Bose, B. Lahmann, J. Pearcy, G. D. Sutcliffe, T. Johnson, F. H. Séguin, C. K. Li, and R. D. Petrasso (Plasma Fusion Science Center, MIT); P. E. Grabowski, B. Bachmann, F. Graziani, H. Whitley, C. Scullard, and L. X. Benedict (LLNL); J. Katz, C. Stoeckl, A. Sorce, C. Sorce, V. Yu. Glebov, and S. P. Regan (LLE); R. C. Mancini (University of Nevada, Reno); and R. Florido (Universidad de Las Palmas de Gran Canaria, Spain)

MIT graduate student P. Adrian and collaborators led an NLUF experiment to study the physics of ion–electron equilibration in high-energy-density plasmas (HEDP's). This work was the basis for an invited talk given at the American Physical Society's Division of Plasma Physics (APS–DPP) meeting in November 2020. In addition, the results for this day and previous NLUF days studying ion–electron equilibration will be published in the 2021 APS–DPP conference proceedings.

Table I: Twenty-one NLUF (in blue) and AIBS (in gray) projects approved for the FY20–FY21 Omega Laser Facility shot allocations.

Principal Investigator	Institution	Title
F. N. Beg*	University of California, San Diego	Charged-Particle Transport and Energy Deposition in Warm Dense Matter With and Without an External Magnetic Field
C. M. Krauland*	General Atomics	Characterization of the Nonlinear Laser–Plasma Interaction in Electron-Assisted Shock Ignition
K. Krushelnick*	University of Michigan	The Dynamics of Strong Magnetic Fields Generated by Relativistic Laser–Plasma Interactions Using OMEGA EP
E. Liang	Rice University	Collision of Two Magnetized Jets Created by Hollow Ring Lasers
R. Mancini*	University of Nevada, Reno	A Laboratory Photoionized Plasma Experiment on OMEGA EP
C. McGuffey	University of California, San Diego	Driving Compressed Magnetic Fields to Exceed 10 kT in Cylindrical Implosions on OMEGA
R. Petrasso*	Massachusetts Institute of Technology	High-Energy-Density Physics, Laboratory Astrophysics, and Student Training on OMEGA
P. Tzeferacos*	University of Chicago	Fundamental Astrophysical Processes in Radiative Supersonic Magnetohydrodynamic Turbulence
M. Valdivia*	Johns Hopkins University	Demonstration of Monochromatic Talbot–Lau X-Ray Deflectometry (TXD) Electron Density Diagnostic in Laser–Target Interactions
J. Wicks*	Johns Hopkins University	High Pressure and Temperature Polymorphism of a Key Super-Earth Mantle Material: MgO
L. Willingale*	University of Michigan	Direct Laser Acceleration of Electrons for Bright, Directional Radiation Sources
M. Cappelli*	Stanford University	Hydrodynamic versus Kinetic Atomic Mix in Deflagrating Converging Plasmas
T. Duffy*	Princeton University	Phase Transitions in Planetary Materials at Ultrahigh Pressures
W. Fox	Princeton University	Magnetic Reconnection in High-Energy-Density Plasmas
R. Jeanloz*	University of California, Berkeley	Multi-Compression and Chemical Physics of Planetary Interiors
H. Ji	Princeton University	Study of Particle Acceleration from Magnetically Driven Collisionless Reconnection at Low Plasma Beta Using Laser-Powered Capacitor Coils
C. Kuranz*	University of Michigan	Experimental Astrophysics on the OMEGA Laser
M. Manuel*	General Atomics	B-Field Effects on Laser–Plasma Instabilities
D. Schaeffer*	Princeton University	Particle Heating by Collisionless Shocks in Magnetized High-Energy-Density Plasmas
B. Srinivasan*	Virginia Tech	Investigation of Feasibility of the 11B(P,3α) Reaction in Inertial Confinement Fusion Settings
W. Theobald*	University of Rochester	Quantifying Turbulent Rayleigh–Taylor Mixing with X-Ray Phase-Contrast Imaging

*Experiments conducted in FY20.

Table II: Graduate students from other universities who have conducted research utilizing the Omega Laser Facility through NLUF, LBS, LaserNetUS, or via collaborations with national labs and LLE in FY20. Eight students successfully defended their Ph.D. theses and one student graduated with an M.S. during Calendar Year 2020 (see the shaded cells).

Name	University	Advisor(s)	Notes
Elizabeth Grace	Georgia Tech	Trebino/Ma (LLNL)	New; LLNL collaboration
Junellie Gonzalez Quiles	JHU	Wicks	
Tylor Perez	JHU	Wicks	
Zixuan Ye	JHU	Wicks	
Patrick Adrian	MIT	Petrasso	
Timothy Mark Johnson	MIT	Petrasso	
Neel Kabadi	MIT	Petrasso	
Justin Kunimune	MIT	Petrasso	
Brandon Lahmann	MIT	Petrasso	
Jacob Pearcy	MIT	Petrasso	
Benjamin Reichelt	MIT	Petrasso	
Graeme Sutcliffe	MIT	Petrasso	
Raspberry Simpson	MIT	Winslow (MIT)/ Ma (LLNL)	LLNL collaboration
Abraham Chien	Princeton	Ji	
Jack Matteucci	Princeton	Bhattacharjee/Fox	Defended Ph.D. thesis in Jan. 2020 (now a freelancer)
Donghoon Kim	Princeton	Duffy	
Sirus Han	Princeton	Duffy	
Ian Ocampo	Princeton	Duffy	
Yingchao Lu	Rice University	Liang	Defended Ph.D. thesis in Oct. 2020 (now a postdoc at the FLASH Center at U. Rochester)
Kyle Perez	Rice University	Liang	New
William Riedel	Stanford	Cappelli	New
Megan Harwell	University of California, Davis	Stewart	New
Roman Lee	University of California, Los Angeles	Mori	New; UCSD-led CMEC GA collaboration (AIBS, M. Manuel)
Mitchell Sinclair	University of California, Los Angeles	Joshi	New; LLNL collaboration (LBS, F. Albert)
Krish Bhutwala	University of California, San Diego	Beg	New
Jacquelynne Vaughan	University of California, San Diego	Beg	New
Joseph Strehlow	University of California, San Diego	Beg	
Shu Zhang	University of California, San Diego	Beg	Defended Ph.D. thesis in July 2020 (now a postdoc at Princeton)

Table II: Graduate students from other universities who have conducted research utilizing the Omega Laser Facility through NLUF, LBS, LaserNetUS, or via collaborations with national labs and LLE in FY20. Eight students successfully defended their Ph.D. theses and one student graduated with an MS during Calendar Year 2020 (see the shaded cells) (continued).

Name	University	Advisor(s)	Notes
Dana Zimmer	University of California, San Diego	Beg	New
Gaia Righi	University of California, San Diego	Meyers	New; LLNL collaboration (PI: C. Stan, H.-S. Park)
Adrianna Angulo	University of Michigan	Kuranz	
Khalil Bryant	University of Michigan	Kuranz	New
Kwyyntero Kelso	University of Michigan	Kuranz	
Heath Lefevre	University of Michigan	Kuranz	
Joseph Levesque	University of Michigan	Drake/Kuranz	Defended Ph.D. thesis in July 2020 (now a postdoc at LANL)
Kevin Ma	University of Michigan	Kuranz	
Michael Springstead	University of Michigan	Kuranz	New
Robert Vandervort	University of Michigan	Drake	
Raul Melean	University of Michigan	Kuranz/McBride	JHU Collaboration (NLUF, P. Valdivia)
Paul T. Campbell	University of Michigan	Krushelnick/ Willingale	Defended Ph.D. thesis in Oct. 2019 (now a FES Postdoc Fellow at U. Michigan)
Brandon Russell	University of Michigan	Krushelnick/ Willingale	
Hongmei Tang	University of Michigan	Willingale/ Krushelnick	
Michael Wadas	University of Michigan	Johnsen	LLNL collaboration (LBS, M. Milliot)
Dylan Cliche	University of Nevada, Reno	Mancini	Defended Ph.D. thesis in Dec. 2020 (now a postdoc at LLNL)
Enac Gallardo	University of Nevada, Reno	Mancini	
Daniel Mayes	University of Nevada, Reno	Mancini	Defended Ph.D. thesis in Dec. 2020 (NNSA CoE postdoc based at SNL)
Ryan P. Schoenfeld	University of Nevada, Reno	Mancini	Graduated in Dec. 2020 with MS
Kyle Swanson	University of Nevada, Reno	Mancini	
Cameron Allen	University of Nevada, Reno	White	New; LLNL collaboration including LBS shots
John J. Donaghy	University of New Hampshire	Fox	New; LaserNetUS
Kevin Meaney	University of New Mexico	Gilmore	Defended Ph.D. thesis in April 2020 (now a Scientist at LANL)

Table II: Graduate students from other universities who have conducted research utilizing the Omega Laser Facility through NLUF, LBS, LaserNetUS, or via collaborations with national labs and LLE in FY20. Eight students successfully defended their Ph.D. theses and one student graduated with an MS during Calendar Year 2020 (see the shaded cells) (continued).

Name	University	Advisor(s)	Notes
Paul King	University of Texas, Austin	Hegelich/Albert	LLNL collaboration including LBS (F. Albert)
Camille Samulski	Virginia Tech.	Srinivasan	New; GA collaboration (NLUF, M. Manuel)
Oliver Vaxirani	Virginia Tech.	Srinivasan	Through LANL collaboration
Victorien Bouffetier	University of Bordeaux	Casner	LLE collaboration including LBS (W. Theobald)
Thomas Campbell	Oxford	Gregori	New; NLUF and LLE collaboration
Hannah Poole	Oxford	Gregori	NLUF and LLE collaboration
Gabriel Perez-Callejo	Oxford	Rose	LLNL collaboration including LBS and HED (E. Marley); Defended Ph.D. thesis in June 2020 (now a postdoc at CELIA, Bordeaux)
Adam Dearing	U. York	Woolsey	New; LLE collaboration (W. Theobald)
Matthew Khan	U. York	Woolsey	RAL/York (PI R. Scott) and LLE collaboration (W. Theobald)
Arun Nutter	U. York	Woolsey	New; Through RAL/York (PI: R. Scott)

JHU: Johns Hopkins University
MIT: Massachusetts Institute of Technology

Many processes in HEDP experiments drive the ions and electrons out of equilibrium. When this occurs, ions and electrons are brought into thermal equilibrium through collisions; however, the equilibration rate can be significantly longer than the dynamical time scale of the plasma. Phenomena such as the structure of shock waves, laser absorption, alpha heating, and magnetic-field advection all depend on the equilibration time scale of ions and electrons. It is critically important when modeling, simulating, or interpreting experiments to have accurate theories calculating ion–electron equilibration. Theories for the equilibration rate must be tested experimentally.

Previously, measurements of ion–electron equilibration in the high-density ($>10^{23}$-cm^{-3}), high-temperature ($>$1-keV) regime were challenging. This work made the first experimental measurements of ion–electron equilibration in this regime by using a novel method to infer ion–electron equilibration rates through low-velocity ion-stopping power measurements. In this regime, most theories predict that the equilibration rate v_{ie} is

$$v_{ie} = \frac{4\pi}{3}\sqrt{\frac{2}{\pi}} \circ \frac{\sqrt{m_e}}{m_i}\left(\frac{Ze^2}{4 \circ \pi \circ \varepsilon_0}\right)^2 \frac{n_e}{T_e^{3/2}}\ln\Lambda. \tag{1}$$

The Coulomb logarithm $\ln\Lambda$ is related to the Coulomb cross section, which must be calculated theoretically. At high density and temperature, the Coulomb logarithm is expected to scale as

$$\ln\Lambda = \ln\left(C\frac{\lambda_{De}}{\lambda_Q}\right), \tag{2}$$

where λ_{De} is the Debye length λ_Q is the De Broglie wavelength, and C is a correction factor that arises in the small angle scattering approximation in the collision physics. All the theoretical uncertainty lies within the calculation of $\ln \Lambda$, so we designed experiments to measure $\ln \Lambda$.

The experiments conducted involved the implosion of thin-glass capsules filled with D^{3}He gas on the OMEGA Laser System. At peak compression, the capsules produce high-density and high-temperature conditions of interest as well as D–D and D–^{3}He fusion reactions. To measure $\ln \Lambda$, our method required an accurate knowledge of the plasma conditions and measurements of the energy loss of the DD-triton and D^{3}He-alpha particles. To measure the plasma conditions, we used x-ray penumbral imaging[1] as well as x-ray spectrometers to characterize the x-ray emission from the capsule. From this data we were able to determine the electron density (n_e) and temperature (T_e) during the thermonuclear fusion phase of the implosion. We also used MIT's charged-particle spectrometers[2] to measure the energy loss of the DD-triton and D^{3}He-alpha particles. From this data we were able to measure an "experimental" Coulomb logarithm $\ln \Lambda_{exp}$.

Figure 1 shows the main result of these experiments. Measurements of n_e and T_e were used to calculate λ_{De} and λ_Q. The probed densities and temperature spanned 1 to 20×10^{23} cm^{-3} and 1.4 to 2.5 keV, respectively. The measured $\ln \Lambda_{exp}$ was then used to constrain the correction factor C from Eq. (2). Figure 1 shows that the best fit is $C = 0.45 \pm 0.14$. Different theories will predict different values for C based on how they handle the small-angle scattering that occurs in ion–electron collisions. After a review of the literature, we have found that three equilibration theories best reflect our measurements. These theories are the quantum Lenard–Balescu (qLB)[3] model, the quantum Fokker–Plank (qFP)[4] model, and the Brown–Preston–Singleton (BPS)[5] model. All three of these models incorporate quantum diffraction into the scattering physics and, according to our data, correctly account for the small-angle collision.

This work demonstrates that the qLB, qFP, and BPS equilibration theories should be used in models and simulations when describing plasma phenomena that occur at high density and high temperature.
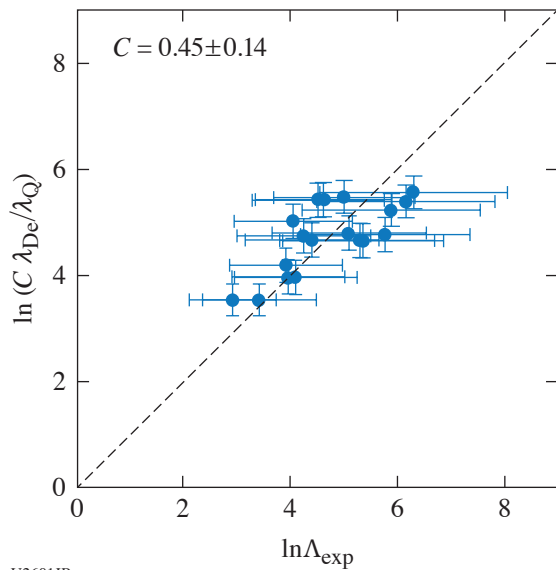

U2601JR

Figure 1

Measurements of the Coulomb logarithm ($\ln \Lambda_{exp}$), Debye length (λ_{De}), and electron thermal De Broglie length (λ_Q) are used to constrain the small-angle scattering correction factor (C). The best fit to the measurements is $C = 0.45 \pm 0.14$. This is consistent with the theoretical predictions of BPS, qLB, and qLF equilibration theories. This result highlights the importance of quantum diffraction and small-angle scattering in predicting the equilibration rate in high-density and high-temperature plasmas.

Applying Laser-Driven Coils for Magnetization of Cylindrical Implosions on OMEGA

Principal Investigators: M. Bailly-Grandvaux, C. McGuffey, and F. N. Beg (University of California, San Diego); J. J. Santos and G. Perez-Callejo (CELIA, University of Bordeaux, France); R. Florido (Universidad de Las Palmas de Gran Canaria, Spain); C. Walsh (LLNL); F. Suzuki-Vidal (Imperial College, UK); R. C. Mancini (University of Nevada, Reno); T. Nagayama (SNL); J. L. Peebles, J. R. Davies, and S. Muller Fess (LLE); M. A Gigosos (Universidad de Valladolid, Spain); and S. Ferri and A. Calisti (Aix-Marseille Université, CNRS, PIIM, France)

Magnetization is one of the possible routes to achieving higher fusion yields in inertial confinement fusion (ICF). Magnetic fields induce anisotropic thermal-electron diffusion, improving energy confinement in the dense core and therefore implosion efficiency, and can therefore decrease the loss of fusion-produced ions, relaxing the areal density constraint of conventional ICF. Yet, demonstrating the viability of magneto-inertial fusion (MIF) requires mastering complex mechanisms such as magnetic-flux compression and nonlocal electron transport.

The experimental campaign aimed at systematically investigating magnetized cylindrical implosions with a quasi-static seed magnetic field (B field) but with a pair of laser-driven Helmholtz-like coils rather than the magneto-inertial fusion electrical discharge system's (MIFEDS) pulsed electrical system. The laser-driven coils present fewer debris and obstruction concerns than MIFEDS, and its scaling is not yet fully explored. The goal of producing a 50-T seed would significantly extend the range of achievable magnetization levels. For the first shot day, we studied the critical issue of B-field compression under well-controlled and monitored conditions of density and temperature using an established cylindrical implosion platform.[6-9] A comparison of imploded plasma has been made with and without a magnetic field. The data obtained will facilitate benchmarking of magnetohydrodynamic modeling and consequently help one to understand the underlying physics of advanced fusion schemes such as the magnetized liner inertial fusion (MagLIF) and astrophysical systems.

The experimental setup used for the four implosion shots is illustrated in Fig. 2. Forty UV beams with a total energy of ~14.5 kJ were delivered in 1.5 ns to compress a cylinder target filled with 11 atm of D_2 + 0.3 at. % of Ar. Three main diagnostics were
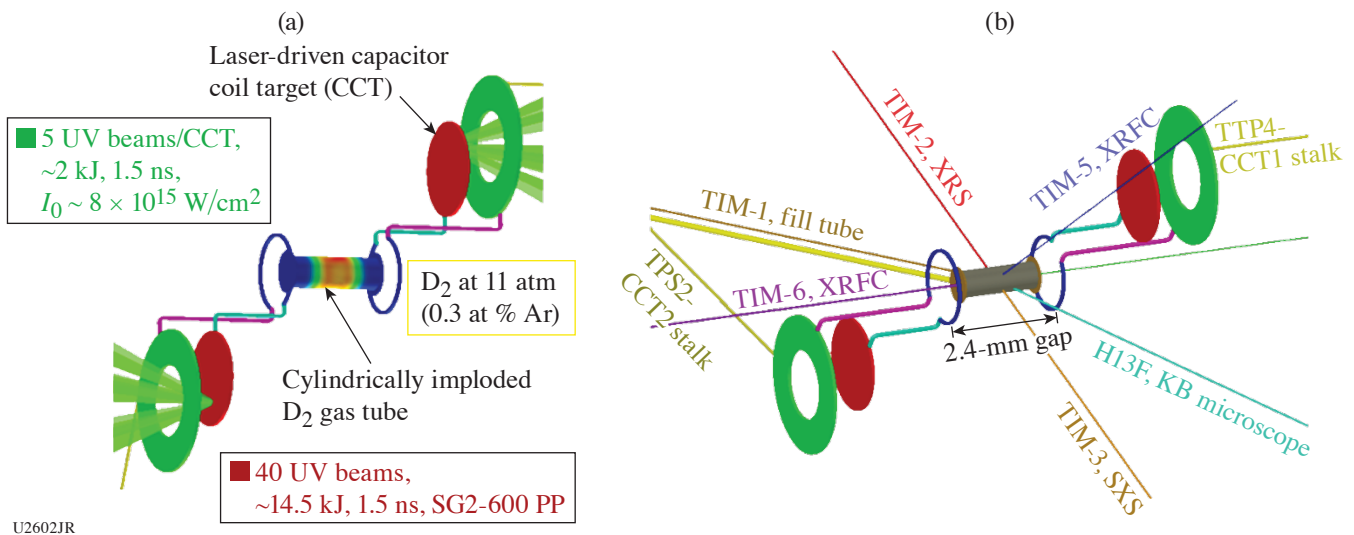

Figure 2

(a) Experimental setup for the "implosion" configuration of the first shot day of the BCoilCompress Campaign. Forty UV beams were used to compress the cylinder target filled with 11 atm of D_2 and 0.3 at. % of Ar. It used the same irradiation scheme as SmallMagLIF. (b) A pair of laser-driven coils in a quasi-Helmholtz configuration was designed for this experiment in order to apply an external magnetic field to the implosion. A total of 2 kJ is delivered in 1.5 ns to each laser-driven coil. CCT: capacitor coil target; TIM: ten-inch manipulator; TPS: Target Positioning System; KB: Kirkpatrick–Baez microscope.

used: (1) a streaked x-ray spectrometer (SXS) using the PJX-2 streak camera, (2) a time-integrated x-ray spectrometer (XRS), and (3) a fast x-ray framing camera (XRFC).

Figure 3 shows the side-by-side results from the x-ray framing camera for (a) a shot with no applied B field and (b) a shot with applied B field. While the magnitude of the externally applied magnetic field with the laser-driven coils is still unknown at this time (the CR-39 proton probing data are being developed and processed by MIT), we can identify signatures that are consistent with the presence of a strong external magnetic field: (1) the magnetized shot emission is brighter and (2) the stagnation in the magnetized case is longer and the target expansion after bang time is significantly reduced. These signatures are in line with the expected magnetic insulation of the heat conduction along the radial direction (perpendicular to the applied B field) and the resulting higher burn temperature. The neutron yields on those two shots were $1.2\pm0.09 \times 10^8$ for the unmagnetized shot and $3.33\pm0.24 \times 10^8$ for the magnetized shot. The neutron-based ion temperature remains unchanged, however, measured at 2.25 keV; yet, neutron measurements are quite sensitive to shot-to-shot variations and further data collection in both conditions will be a focus of the next shot day.
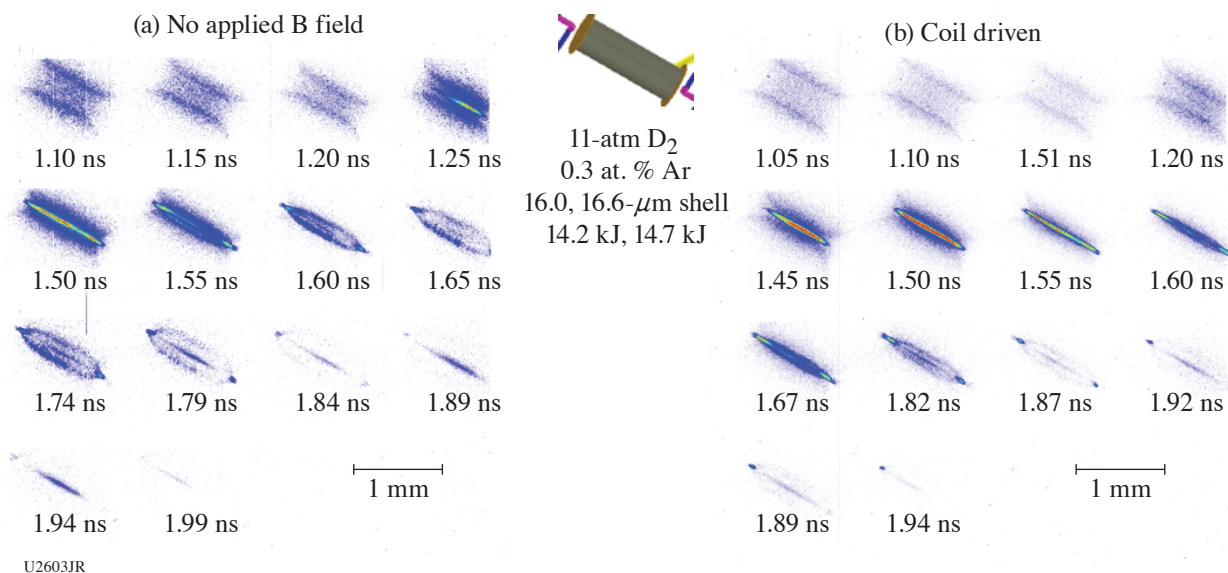
Figure 3

Results from the x-ray framing camera in TIM-5 for (a) shot 98882 (no applied B field) and (b) shot 98885 (coil driven). The two images are displayed with the same color bar and the acquisition settings were identical. Typical signatures of an applied magnetic field are observed in the shot with driven coils, namely (1) a brighter x-ray emission, (2) a longer stagnation, and (3) a slower disassembly of the target after maximum compression.

We performed 1-D and 2-D extended-magnetohydrodynamic (MHD) simulations using the code *GORGON*[10] to study the effect of the applied B field on the implosion. The history of plasma conditions from *GORGON* are used to calculate the time-dependent emission from the Ar dopant, using the collisional-radiative atomic kinetics code ABAKO[11] and Stark-broadened line shapes from the MERL code.[12] Synthetic time-resolved emission of the Ar dopant is shown in Fig. 4. The 50-T applied B field is strong enough to modify the plasma conditions of the compressed core throughout the implosion. The higher burn temperature, lower burn density, and longer stagnation time of the magnetized case affect the line ratios, the line widths, and the duration of the emission, respectively.

(a) B$_{seed}$ = 0 T

(b) B$_{seed}$ = 50 T

Spatial gradients change the streaked emission pattern

Ly$_\gamma$ (4p→1s)
Ly$_\beta$ (3p→1s)
He$_\gamma$ (1s4p→1s^2)
He$_\beta$ (1s3p→1s^2)
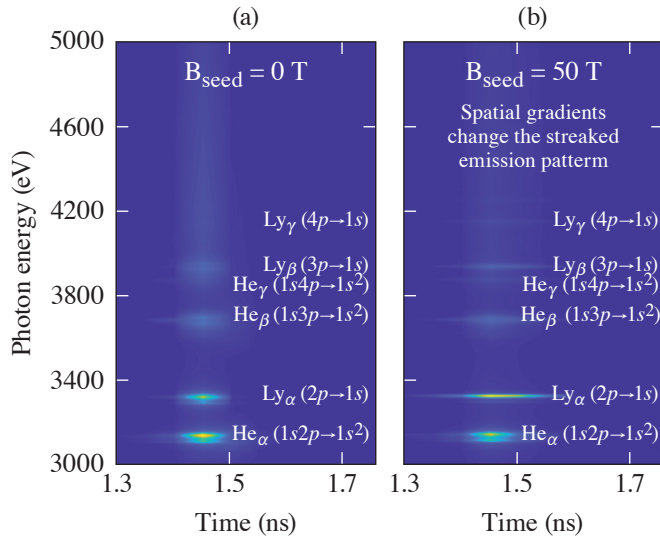Ly$_\alpha$ (2p→1s)
He$_\alpha$ (1s2p→1s^2)

U2661JR

Figure 4
Synthetic time-resolved emission of the Ar dopant, calculated for (a) an unmagnetized (B$_{seed}$ = 0 T) implosion and (b) a magnetized (B$_{seed}$ = 50 T) implosion.

Strongly Magnetized Shock-Driven Implosions on OMEGA

Principal Investigators: A. Bose, N. V. Kabadi, P. J. Adrian, G. F. Sutcliffe, J. A. Frenje, M. Gatu Johnson, C. K. Li, F. H. Séguin, and R. D. Petrasso (Plasma Science and Fusion Center, MIT); J. L. Peebles, F. J. Marshall, C. Stoeckl, S. P. Regan, V. Yu. Glebov, J. R. Davies, R. Betti, S. X. Hu, and E. M. Campbell (LLE); C. A. Walsh, H. Sio, and J. Moody (LLNL); A. Crilly, B. D. Appelbe, and J. P. Chittenden (Imperial College, UK); and S. Atzeni (Sapienza, University of Rome)

In these experiments, we imposed a very high, 50-T initial magnetic field on shock-driven implosions to produce strongly magnetized ion plasma conditions, i.e., with ion Hall parameter $\chi_i \sim 5$. At these conditions, the electrons are also strongly magnetized, with an electron Hall parameter (χ_e) of ~45. Magnetization of electrons suppresses cross-field electron thermal transport and enhances the mode-2 asymmetry in the implosions. We observed the change in implosion shape with magnetization in x-ray self-emission images. This platform will be used to study ion kinetic effects, which scales with the ion Hall parameter as $\sim 1/\chi_i$, and the impact of ion viscosity $\left(\sim 1/\chi_i^2\right)$ on the implosion dynamics.

We imploded thin glass shells, shown in Fig 5, filled with a low-density gas, using 40 OMEGA beams in a polar-direct-drive configuration. Laser beam repointing was not applied in these experiments. A 50-T external magnetic field was applied with a current-carrying coil going around the target. A wide range of diagnostics were fielded on OMEGA for measurements of ion and electron temperature, implosion convergence, and implosion shape.

We measured an electron temperature of ~2 keV using an x-ray spectrometer, an ion temperature of ~11 keV from multiple neutron time-of-flight (nTOF) and charged-particle (T^{3}He-d and D^{3}He-p) spectrometers, and a convergence in implosion radius by a factor of ~4× from time-resolved x-ray self-emission images. The initial 50-T B field was flux compressed to ~8 MG, which is a 16× field amplification. A large magnetic Reynolds number of ~1000, estimated from the measurements, allows an effective flux compression in these implosions.

The condition for magnetization is given by the Hall parameter $\chi > 1$:

$$\chi = \frac{\lambda_{mfp}}{r_g} \propto \frac{T^{3/2}B}{m^{1/2}n} > 1, \tag{3}$$

which scales with the temperature (T), B field (B), mass (m) of the plasma species (electrons or ions), and number density (n). We produced an electron Hall parameter of ~45, significantly higher than $\chi_e \sim 2$ produced in more-compressive magnetized ICF implosions on OMEGA.[13] We produced plasma conditions with strongly magnetized ions $\chi_i \sim 5$. A spherically converging shock
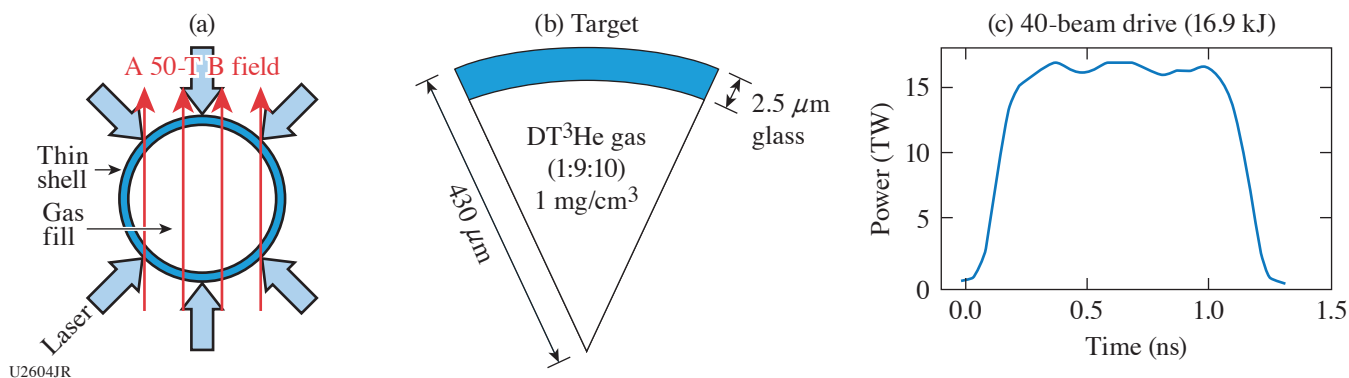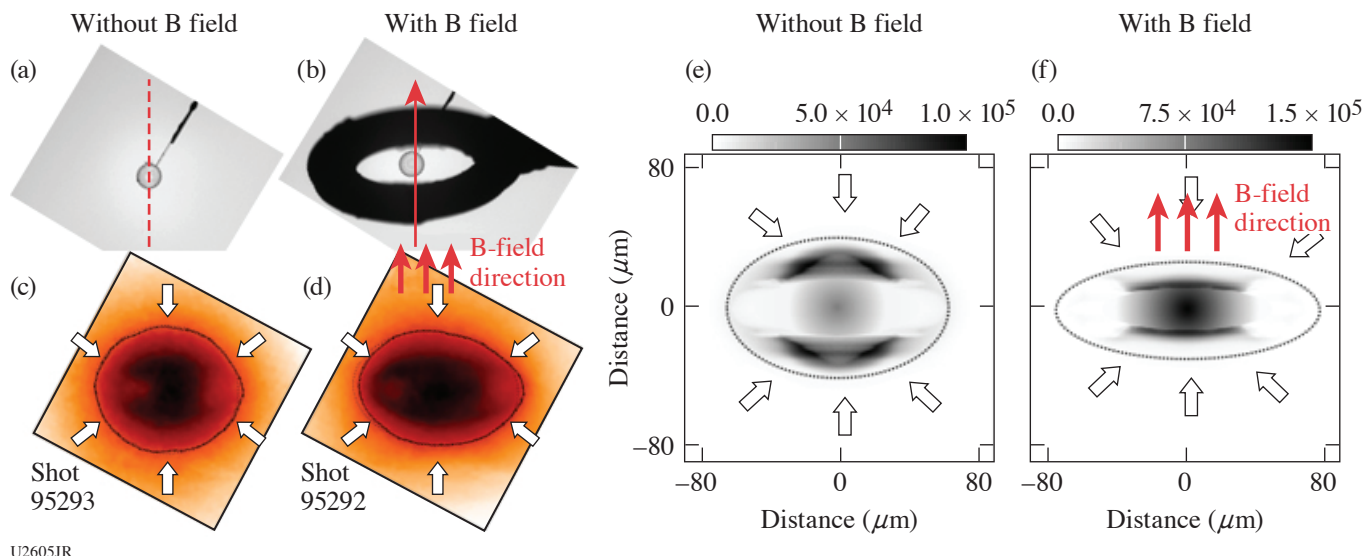
Figure 5
The experimental configuration on OMEGA: (a) a 50-T externally imposed initial B field was imposed on a target driven with 40 beams in a polar-direct-drive configuration. (b) Thin glass targets with a gas fill were used. (c) A 1-ns square pulse was used to drive the implosions.

differentially heats up the ions of the plasma to very high temperatures (~11 keV), and since the ion Hall parameter [Eq. (3)] scales as a high power of temperature $T^{3/2}$, strongly magnetized ions could be produced in these experiments. The fuel ion magnetization conditions we produced are comparable to MagLIF experiments $\chi_i \sim 1$ (Ref. 14). Experiments on OMEGA provide a wide selection of diagnostics and a clear field of view of the implosion, allowing complementary and high-fidelity measurements of the strongly magnetized implosion properties.

It is observed for the first time that strong magnetization can enhance the mode-2 asymmetry in implosions. Figure 6 shows a comparison between a nonmagnetized shot on the left and a magnetized shot on the right. A current-carrying coil going around the target, shown in Fig. 6(b), produces the 50-T imposed B field. The B-field direction, which is along the coil axis, coincides with the laser-drive axis. It can be observed from a comparison of the x-ray self-emission images [Figs. 6(c) and 6(d)] that external magnetic fields enhance the mode-2 asymmetry, making it more elliptic in shape. The compression is suppressed along the waist, i.e., in the direction perpendicular to the imposed B field. This is because the B field introduces an

Figure 6
A comparison between nonmagnetized (left) and magnetized (right) implosions. The [(a),(b)] experimental geometry, [(c),(d)] x-ray self-emission images, and [(e),(f)] preliminary simulation images are shown.

anisotropy in transport properties between the directions parallel and perpendicular to the field. In the direction perpendicular to the B field, the thermal conduction is suppressed $\left(\sim 1/\chi_e^2\right)$, whereas in the direction parallel to the B field, the conductivity is unaltered. X-ray self-emission images from *GORGON* simulations in Figs. 6(e) and 6(f) show qualitative agreement in shape with the experiments.

Sponsored by the DOE–NNSA NLUF Program on OMEGA, these experiments are the first strongly magnetized shock driven implosions, and a part of platform development effort for future experiments to study effects of strongly magnetized ion and electrons on the plasma transport properties and effects on ICF implosion dynamics with an externally imposed B field.

This material is based upon work supported by the Laboratory for Laser Energetics, University of Rochester, and by the DOE/NNSA CoE at MIT with Contract DE-NA0003868.

High-Pressure Polymorphism of Gold Under Laser-Based Ramp Compression to 690 GPa

Principal Investigators: S. H. Han, D. Kim, J. K. Wicks,[*] and T. S. Duffy (Princeton University); R. F. Smith, A. Lazicki, and J. H. Eggert (LLNL); and J. R. Rygg (LLE)
[*]Now at Johns Hopkins University

Gold is a 5d transition metal with widespread use in high-pressure science. Recently, considerable attention has been paid to its phase behavior at multimegabar conditions. Theoretical studies have predicted 300-K transformations from the ambient face-centered cubic (fcc) structure to a hexagonal close-packed (hcp) structure at pressures ranging from 151 to 410 GPa (Refs. 15–18), followed by a second transformation to a body-centered cubic (bcc) phase[16,18] from the fcc to a double-hexagonal close-packed (dhcp) phase at pressures between 232 and 250 GPa (Refs. 19 and 20), or to a series of stacking disordered phases above 390 GPa (Ref. 21).

Two of these phases have been experimentally observed: experiments in an electrically heated diamond anvil cell first observed the hcp phase at 248 GPa and 800 K (Ref. 20). Other experiments using newly developed anvil designs reported only the fcc phase up to as high as 1.06 TPa under room-temperature compression.[22] Laser-based shock-compression experiments coupled with *in-situ* synchrotron x-ray diffraction experiments have recently shown that gold transforms to the bcc phase under shock loading, coexisting with the fcc phase and then a liquid phase along the Hugoniot.[23,24]

To test off-Hugoniot polymorphism, we performed laser-based ramp compression on gold. Target packages were constructed using a 2.5-μm-thick layer of gold, diamond ablators, and either diamond or LiF windows. For higher-stress experiments, a 1-μm-thick layer of gold was included in the ablator in order to shield the sample from x rays generated by the ablation plasma. The experiments used Cu backlighters and either Pt, W, or Ta pinholes. Samples were compressed on both OMEGA and OMEGA EP using laser-ablation ramp compression and characterized using the powder x-ray diffraction image plate (PXRDIP) and velocity interferometer system for any reflector (VISAR) diagnostics.

A total of eight experiments were successfully conducted: two on OMEGA EP and six on OMEGA. The gold samples were sampled at stresses between 166 and 690 GPa. Pressures were determined using either the method of characteristics or forward modeling using hydrocode simulations. Between one and three diffraction lines were observed in each experiment, consistent with diffraction from the fcc phase, the bcc phase, or a mixture of the two [see Fig. 7(a)]. Diffraction from shots between 166 and 259 GPa is consistent with just the fcc phase, while between 299 and 333 GPa, asymmetry of the most-intense diffraction peak is consistent with diffraction from both the fcc (111) and the bcc (110). Between 377 and 690 GPa, the diffraction is consistent with just the bcc phase.

Our results indicate that gold transforms to the bcc phase at thermodynamic states intermediate between the 300-K isotherm and the Hugoniot. Temperatures were not directly measured in these experiments, but were constrained from above by the melt curve due to the presence of crystalline diffraction, and from below by a modified isentrope. The lower boundaries to these temperature estimates are slightly higher than the theoretically calculated boundaries for the hcp phase [see Fig. 7(b)].
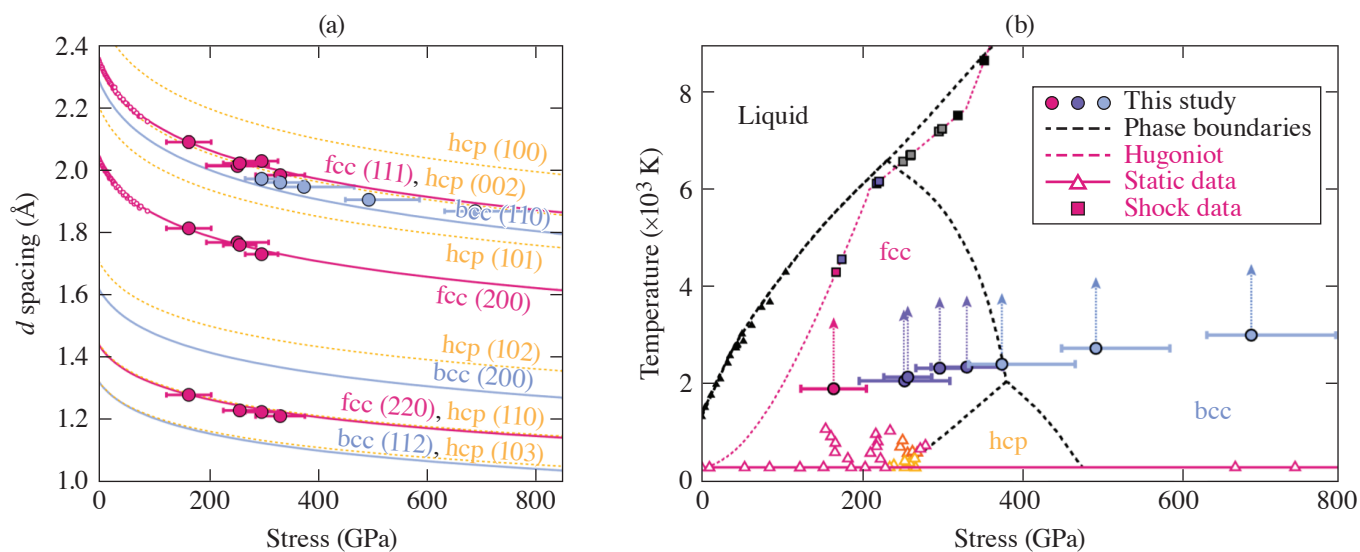
Figure 7

(a) Observed *d* spacing as a function of stress. Circles indicate phase assignment for a given data peak (magenta = fcc, blue = bcc). Uncertainty in *d* spacing is smaller than the size of the data marker. Solid and dotted lines represent ideal diffraction at 300 K calculated using equation-of-state data from Refs. 16 and 22. For the hcp phase, for which no equation-of-state data exist, fcc parameters were used instead. Increased observed *d* spacing relative to these calculations is likely a result of heating. Magenta circles represent static-compression diffraction data.[25] (b) The color of the data point corresponds to phase assignment: magenta = fcc, blue = bcc, purple = mixed fcc/bcc, yellow = hcp, orange = mixed hcp/fcc, gray = mixed liquid/bcc, black = liquid. Upward-pointing arrows indicate that these are lower boundaries to the temperature. Theoretically calculated phase boundaries are from Ref. 16, static data from Refs. 20 and 26, and shock data from Refs. 23 and 24.

Performance Scaling in Inverted-Corona Neutron Sources

Principal Investigators: M. Hohenberger, N. Meezan, and A. J. Mackinnon (LLNL); N. Kabadi (Plasma Science and Fusion Center, MIT); W. Riedel and M. Cappelli (Stanford University); S. Glenzer (SLAC); and C. Forrest (LLE)

Experiments were conducted to explore the physics of inverted-corona neutron sources. Here, laser beams are incident onto the inside surface of a sphere through one or more laser entrance holes (LEH's), thereby ablating a layer of fusion fuel on the inner surface of the target, e.g., a CD (deuterated plastic) liner.[27] Fuel may also be provided as a gas fill, with the laser-driven ablation launching a centrally converging shock into the gas. In either case, the fusion fuel stagnates on center and is heated to fusion conditions. Such targets have shown promise as neutron sources for high-energy-density applications with relaxed symmetry requirements. Prior experiments demonstrated a strong yield dependence on the CD-liner thickness, contrary to simulations, indicating substantial mix in the ablating plasma.[28]

Targets with a 1.8-mm inner diameter and 20-μm-thick walls were laser irradiated by 40 OMEGA beams through two LEH's with 1-ns square pulses and 500 J/beam [see Fig. 8(a)]. The shot day comprised three parts: (1) scanning the gas-fill density utilizing CH-wall targets and a D_2-gas fill to test yield dependence on pressure; (2) combining CD-lined targets with a ^{3}He gas fill to diagnose the mix between wall plasma and gas fill via the proton emission from D–^{3}He fusion reactions; and (3) characterizing yield scaling with CD-liner thickness in a vacuum target to quantify ablatively driven mix in the wall expansion. Except for the gas-fill density data, all experiments required a CD liner to drive either D–D or D–^{3}He fusion reactions as the primary experimental signature. Unfortunately, an error in the target build resulted in the CD layer on the outside of the target, rather than the inside, and therefore physically separated from the interaction region of interest [see Fig. 8(b)]. Consequently, only the gas-fill scan provided useful data.
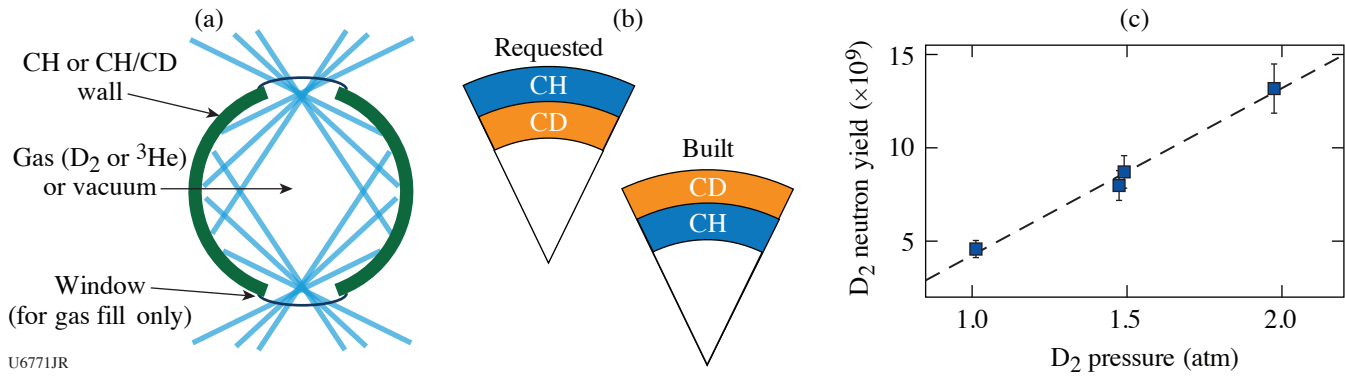
Figure 8

(a) The capsule is laser irradiated on the inside surface via two laser entrance holes, thereby driving a wall expansion with central stagnation, heating the fuel to fusion conditions. (b) An error when building the target resulted in a CD liner on the outside of the capsule, rather than on the inside as requested. (c) For the gas-filled CH targets, the fusion yield scales linearly with the fill pressure, as expected.

Neutron yield versus fill pressure is shown in Fig. 8(c). Ignoring any impact from mix of non-fusionable wall material into the gas, yield is expected to scale linearly with fill density, $Y \sim \rho$, consistent with the data in Fig. 8(c). It should be noted that the fit is offset from the origin, which may be interpreted as a minimum gas fill to hold back expansion of the non-fusionable wall into the central hot region. Further analysis and simulations are in progress.

Overview of Collisionless Shock Experiments Using a Gas Jet on OMEGA

Principal Investigators: T. M. Johnson, J. A. Pearcy, A. Birkel, G. D. Sutcliffe, and C. K. Li (Plasma Science and Fusion Center, MIT)

Generation of astrophysically relevant, electromagnetic collisionless shocks in a laboratory has been an important experimental goal during the last several decades for scientists wanting to explain numerous fascinating astrophysical phenomena and to study the fundamental physics of particle acceleration.[29] Astrophysically relevant shocks are usually magnetized, have high plasma β (ratio of the thermal plasma pressure to the magnetic-field pressure) and low collisionality, and are super Alfvénic (Alfvénic Mach number $M_A > 2$ to 3). In particular, the strong magnetic fields are spontaneously generated by plasma instabilities, which scatter and reflect incoming particles out of the thermal pool from the shock ramp to the upstream, providing essential mechanisms for shock energy dissipation. Numerous experiments have been performed with various advanced concepts and configurations, including the counter-streaming supersonic plasma flows or driving a supersonic plasma flow (piston) into and compressing a pre-magnetized background plasma.

Sponsored by the DOE/NNSA NLUF Program on OMEGA, we have started a project to systematically study the laboratory generation of collisionless shock and particle acceleration through driving a magnetized, supersonic plasma flow into a target object. These targets include a gas bag,[30] a solid plastic sphere, and a gas volume from a gas jet. Figure 9(a) is a schematic of the experimental setup for the gas-jet experiment (pMagShock-20A), where a highly collimated plasma flow was generated by six laser beams (total energy ~3 kJ) illuminating the interior of a plastic (CH), hemispherical target. The supersonic plasma flow interacts with a pre-ionized hydrogen gas jet, forming a magnetized electromagnetic shock. Since the ion mean free path is much larger than the shock width, the formed shock is collisionless. A number of important plasma diagnostics have been used to measure and characterize this experiment, including 2ω Thomson-scattering measurements, proton radiography, and multichannel electron spectrometry. Typical experimental results are shown in Fig. 9. The Thomson-scattering measurement in Fig. 9(b) indicates that the plasma flow has a velocity of ≥ 1000 km/s, density of $\sim 10^{19}/cm^3$, and electron temperature of ~200 eV. Figure 9(c) shows a side-on image with 15-MeV monoenergetic backlighting protons, providing the visualization of plasma shock structure and filaments. Figure 9(d) shows an electron spectrum with a nonthermal tail, indicating a power-law distribution with a slope of ~3. A number of physical mechanisms have been proposed for such observed shock acceleration, including the first-order (diffusive) acceleration and the second-order Fermi (stochastic) acceleration, shock-drift acceleration, shock-surfing acceleration, and ripple-
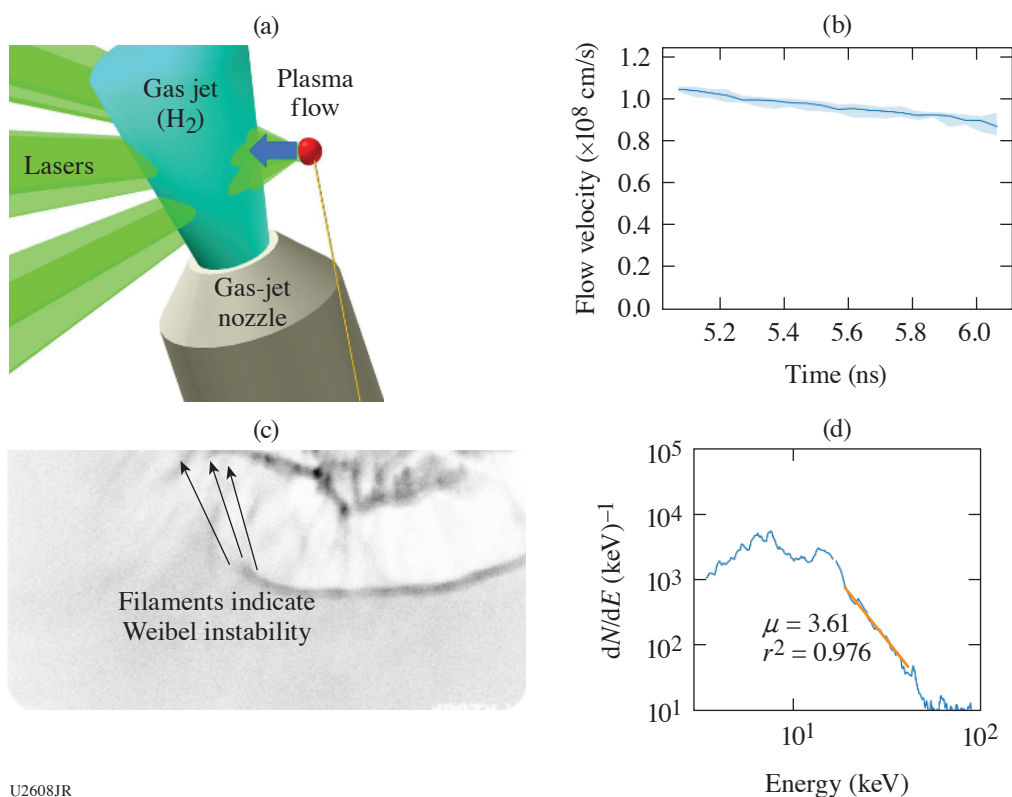
U2608JR

Figure 9

(a) Schematic of the experimental setup. (b) Thomson-scattering measurement indicating that the plasma flow has a velocity of ≥1000 km/s, a density of ~10^{19}/cm³, and an electron temperature of ~200 eV. (c) A side-on image with 3-MeV monoenergetic backlighting protons providing the visualization of plasma shock structure and filaments. Darker areas are more protons. (d) An electron spectrum with a nonthermal tail, indicating a power law distribution with a slope of ~3.

shock acceleration. On this shot day, a total of 12 shots were performed with different plasma conditions and measured with all diagnostics at different times and different locations. Currently we are focusing on systematically analyzing all experimental data. In the meantime, we are performing comprehensive numerical simulations including using *FLASH* hydrodynamic simulations to model the supersonic plasma flow generation and propagation and *OSIRIS* particle-in-cell simulations to model the generation of plasma ion Weibel filaments and formation of electromagnetic shocks. The experiments directly mimic the scenario of collisionless shocks in nonrelativistic astrophysical contexts, such as in the supernova remnants, and provide a roadmap for studying shock physics in relativistic regimes, such as in the afterglow of cosmological γ-ray bursts.

High-Energy-Density Physics and Planetary Evolution

Principal Investigators: Y.-J. Kim, M. Millot, P. M. Celliers, J. H. Eggert, and D. E. Fratanduono (LLNL); J. R. Rygg and G. W. Collins (LLE); S. Brygoo and P. Loubeyre (CEA, France); and R. Jeanloz (University of California, Berkeley)

Our NLUF collaboration aims at documenting the microscopic properties and new chemical physics behavior of low-Z materials that are the key constituents of gas giant planets and exoplanets, namely hydrogen, helium, and hydrogen–helium mixtures.[31]

In FY20, we conducted the DACplanetEP-20A Campaign with diamond-anvil-cell (DAC) targets in a direct-drive geometry for a total of 12 shots on OMEGA EP. New technical developments with the DAC targets were demonstrated to reach higher-pressure regimes and obtain multiple shock data from a single experiment. First, a 10-ns-long drive duration, instead of the usual 1- to 3-ns drive, was tested with a DAC having a wide aperture [Fig. 10(a)]. Next, reverberation of a shock wave was generated by a tungsten

layer to provide two different shock Hugoniot states in a sample. Finally, we demonstrated that preparing thick precompressed samples allows us to carry out decaying-shock measurements, paving the way for future experiments on H–He mixtures.[32]

Doppler velocimetry (VISAR) and streaked optical pyrometry (SOP) were used to monitor the shock-wave propagation through the transparent, precompressed sample and to document the pressure–density–temperature shock equation of state as well as the evolution of the optical properties (reflectivity, absorption coefficient) using a quartz reference [see Figs. 10(b) and 10(c)].[33] Ongoing data analysis is being used to improve our measurements, allowing us to explore a new regime of matter that will be useful for benchmarking future equation-of-state and planetary models.
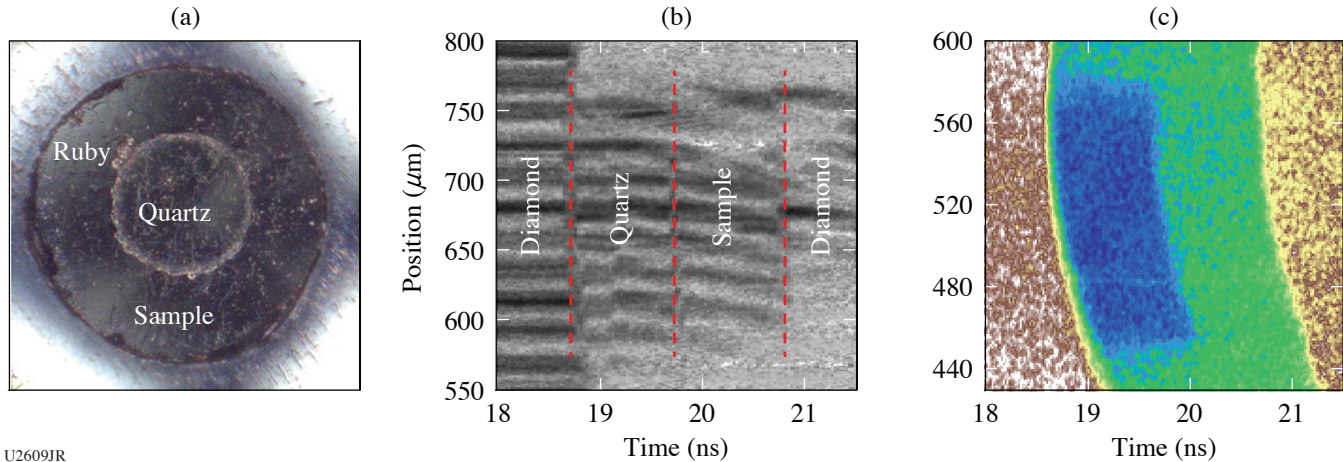
Figure 10
(a) A sample chamber image of the wide-aperture DAC; (b) VISAR; and (c) SOP data obtained from a long drive experiment.

Characterization of the Nonlinear Laser–Plasma Interaction in Electron-Assisted Shock Ignition

Principal Investigators: C. Krauland and A. Raymond (GA); K. Matsuo, D. Kawahito, and F. N. Beg (University of California, San Diego); S. Zhang (Princeton University); and A. Hansen, J. Katz, and W. Theobald (LLE)

Shock ignition (SI) has been proposed as an alternative approach to ICF. The SI approach separates the compression and ignition processes, using a low-intensity pulse to implode the fuel capsule, followed by a high-intensity laser spike to generate a strong convergent shock to trigger ignition. The spike in the laser pulse shape is of sufficiently high irradiance to cause strong laser–plasma instabilities (LPI's). The resultant hot electrons with moderately high temperature (<100 keV) are predicted to benefit the SI scheme by enhancing the ignition shock.[34]

We completed experiments on the OMEGA laser at the end of FY20 to characterize the shock propagation and plasma parameters in our previously established SI-relevant planar geometry experimental platform. Twenty UV beams partially overlapped in space produce a large-scale-length (>300-μm) and high-temperature (>keV) coronal plasma.[35] In some shot cases, with the aid of a shaped laser pulse, a high-intensity ($I \sim 10^{16}$ W/cm^2) laser interaction followed. Figure 11(a) shows a schematic of this platform with the two laser power profiles fielded [Figs. 11(b) and 11(d)]. On this shot day, a SOP and VISAR were used to measure the shock breakout time and to track shock fronts moving in the target, respectively. Figures 11(c) and 11(e) compare the SOP measurements with each pulse shape. In the case with the spike, the shock front reaches the rear surface of the target 1.2 ns earlier than the case without the spike pulse. Compared to our previous OMEGA EP experiments that fielded only a single UV beam to produce the high-intensity interaction, this 20 overlapped-beam setup at the same peak intensity shows better laser-shock energy coupling. Previous SOP measurements showed a delta of only 0.2 ns. Bremsstrahlung data also suggest that the overlapped UV lasers produce more hot electrons than a single UV beam of comparable intensity by a conversion efficiency increase of >2×. We performed simulations to validate experimental SOP/VISAR data using the code *FLASH*,[36] which estimated peak ablation pressures ~90 Mbar for the shots with a spike pulse in the overlapped-beam platform.

To verify modeling of the plasma conditions with and without a high-intensity UV beam interaction, a 4ω probe beam was also utilized for Thomson scattering. We probed both the coronal plasma and the high-intensity interaction at various distances from the initial target surface, ranging from 300 to 1100 μm, corresponding to plasma densities between n_c to $n_c/10$. While the analysis is ongoing, an example of the electron plasma wave (EPW) and ion acoustic wave (IAW) data is presented in Fig. 12,
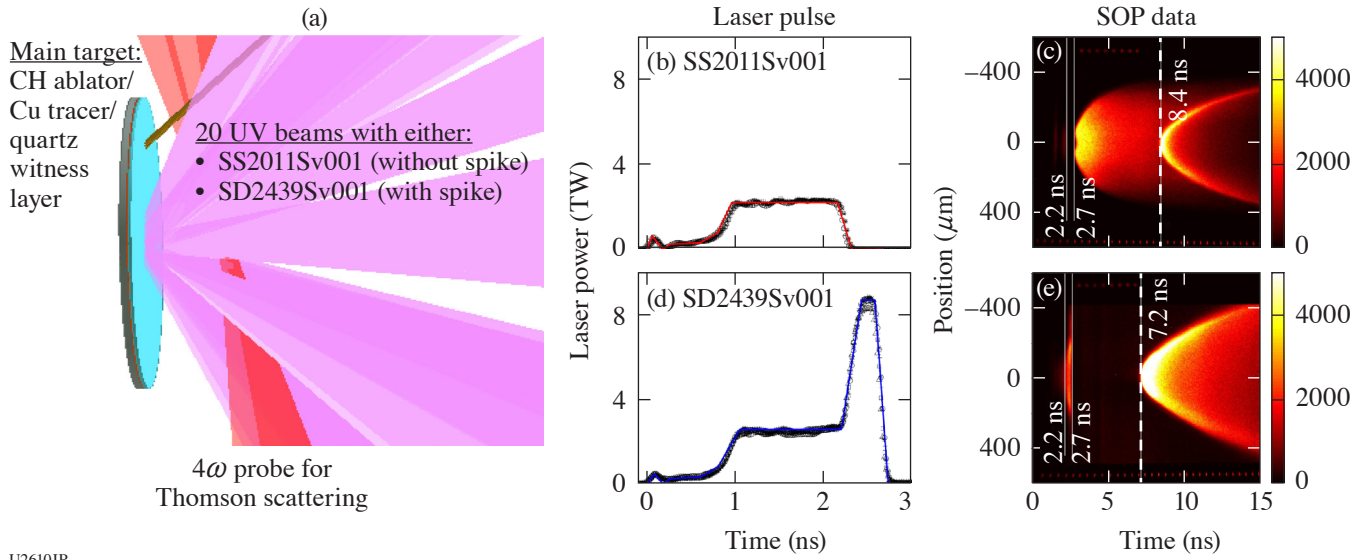
U2610JR

Figure 11

(a) OMEGA experimental platform with [(b),(d)] the utilized laser pulses. [(c),(e)] Measured SOP data can be seen in the case where a low-intensity drive creates an SI-relevant plasma (top row) and the case where a high-intensity spike pulse is injected (bottom row).
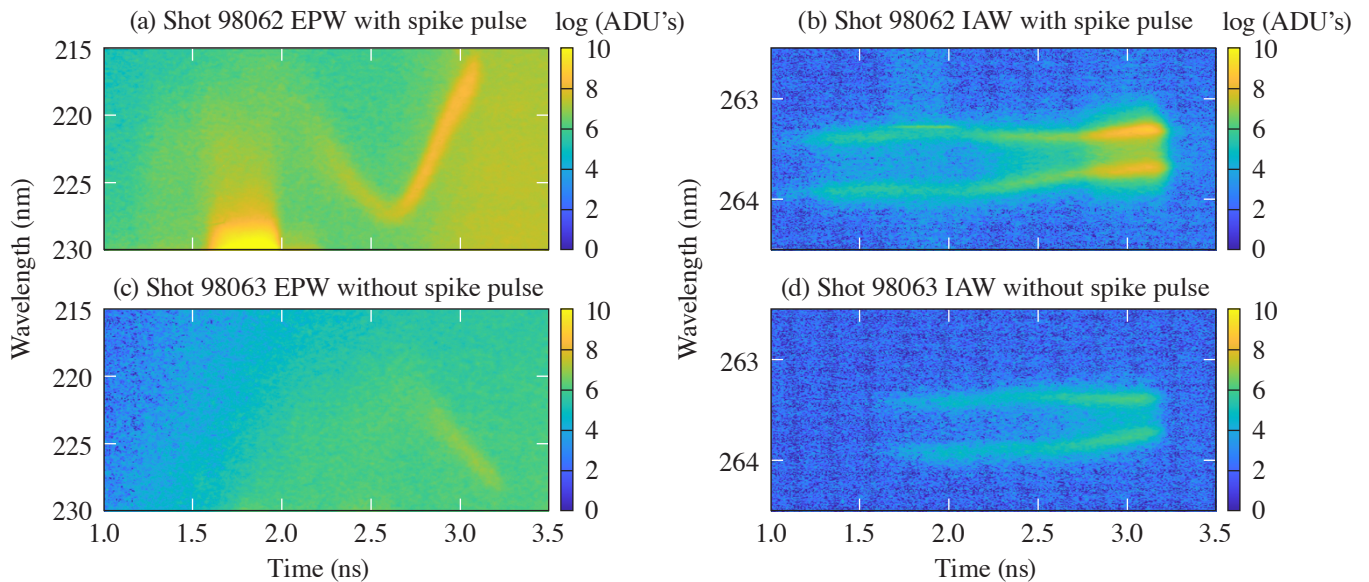
U2611JR

Figure 12

[(a),(c)] Measured EPW and [(b),(d)] IAW features measured using the OMEGA Thomson-scattering system at a 4ω probe standoff of 700 μm (corresponding to $n_c/4$). Shot 98062 utilized a spike pulse shape and shot 98063 did not.

corresponding to a focal standoff of 700 μm $(n_c/4)$. Qualitatively, the data indicate an expected increase in plasma temperature during irradiation by the spike pulse; the measured values of the temperatures and density will be compared to expectations from *FLASH* modeling when analysis is complete. These direct measurements of SI-relevant plasma conditions will also serve to seed initial plasma conditions in ongoing particle-in-cell simulations aimed at investigating the LPI.

Experiments to Observe Laboratory Photoionization Fronts in N Gas Cells

Principal Investigators: H. J. LeFevre, K. Kelso, J. S. Davis, W. J. Gray, R. P. Drake, S. R. Klein, and C. C. Kuranz (University of Michigan); and P. A. Keiter (LANL)

Ionizing radiation has been present in the universe since the age of reionization, approximately 200 million years after the Big Bang, until the present day. The emission that escaped from the first galaxies provided the photon flux to drive the reionization of the intergalactic medium in photoionization fronts.[37] Additionally, in present day astrophysics, the ionizing radiation from the forward shock in type-IIn supernovae drives a photoionization front that heats the circumstellar medium, which affects the behavior of the light curve and causes the appearance of narrow lines in the emission spectrum.[38] Experiments on the OMEGA laser study the formation and structure of photoionization fronts to better understand the reionization of the early universe and the evolution of supernovae.

A photoionization front is a heat front where photoionization is the dominant heating mechanism at the interface between the hot downstream and cold upstream material. The heated downstream sufficiently reduces the opacity such that the radiation transport in this region is nondiffusive, which presents an interesting challenge to many radiation-hydrodynamic codes. Drake *et al.*[39] and Gray *et al.*[40] explore the requirements for producing this type of heat front in a high-energy-density physics facility and provide two dimensionless ratios of atomic rate coefficients to determine the physics regime of an experiment. The first of these ratios is

$$\alpha = \frac{n_{i+1}}{n_i} \frac{n_e R_{i+1,i}}{\Gamma_{i,i+1}}, \tag{4}$$

where n_i is the ion number density of the ith ionization state in cm^{-3}, n_e is the electron number density in cm^{-3}, $R_{i+1,i}$ is the recombination rate coefficient in cm^3 s^{-1}, and $\Gamma_{i,i+1}$ is the photoionization rate in s^{-1}. The second dimensionless parameter is

$$\beta = 1 + \frac{n_i}{n_{i+1}} \frac{\langle \sigma v \rangle_{i,i+1}}{R_{i+1,i}}, \tag{5}$$

where $\langle \sigma v \rangle_{i,i+1}$ is the electron collisional rate coefficient in cm^{-3} s^{-1}. To produce a photoionization front, an experiment needs values of $\alpha \ll 1$ and $\beta \sim 1$.

Ph.D. students H. LeFevre and K. Kelso designed and ran the shot days for these experiments using a 2- to 4-atm N gas cell with 1% Ar, by mass, as a spectroscopic dopant for the propagation medium and the soft x rays from the rear surface of a laser-irradiated Au foil as the ionizing radiation source. The gas cell was 3-D–printed plastic with a 3-mm × 3-mm-sq cross section and 7-mm length of gas volume. The Au foil was 500 nm thick and sat 400 μm from the front of the gas cell with an incident laser intensity of 10^{14} W/cm^2. Windows are printed into the gas cell for diagnostic access with the center point 1350 μm from the Au foil. These rectangular windows are 0.6 mm along the propagation direction of the photoionization front and 2 mm in the other dimension with 3-μm mylar foils to seal in the gas but allow few-keV x rays to pass through. This design improved upon previous designs since it was more capable of holding gas at these pressures and allowed for a larger spectral range of the primary diagnostic.

The primary diagnostic in this experiment is streaked x-ray absorption spectroscopy of the Ar K shell. A capsule implosion acts as a continuum source in the 2- to 4-keV range for the Ar absorption measurements. H. LeFevre recently submitted a publication to Review of Scientific Instruments detailing the characterization and performance of CH vacuum capsules as x-ray backlighters under anisotropic laser irradiation from previous NLUF experiments. These most-recent experiments tested a new capsule backlighter design that uses a 200-nm layer of Ni on the interior surface of an ~7-μm-thick CH layer with an outer diameter of 870 μm. The intent of this design is to produce two useful spectral regions with a single source: continuum emission in the 2- to 5-keV range and line emission from the Ni K shell around 7.8 keV.

A day of experiments in August 2020 tested the new backlighter and made streaked spectral measurements through the gas cell. The Ar dopant percentage was too low to clearly distinguish any absorption features during these experiments. This further demonstrates, however, that the new gas-cell design was a success and solved the issue with collimating the absorption source in the previous shot day, even though the data were not as expected. Increasing the Ar fraction easily resolves this issue and suggests that the next shot day should produce excellent data. There were very promising results for the new backlighter design. There was strong continuum in the 2- to 4-keV range on a time-integrated spectrometer used as an unattenuated reference to compare with the streaked absorption spectra shown in Fig. 13(a). Emission in the 5- to 8-keV range on a second time-integrated spectrometer saw weak line structures from the Ni K shell. Figure 13(b) shows the contrast-enhanced raw data clearly indicating line emission. Figure 13(c) shows the detailed features of the Ni line emission. Ideally, this would be much stronger if one intends to use these lines to probe a plasma of interest, but this is a good starting point for a first shot day with a new design. Future experiments will reduce the capsule mass to allow for larger implosion velocities, which should increase the temperature of the Ni and result in stronger line emission.

(a) Time-integrated low-energy spectrum

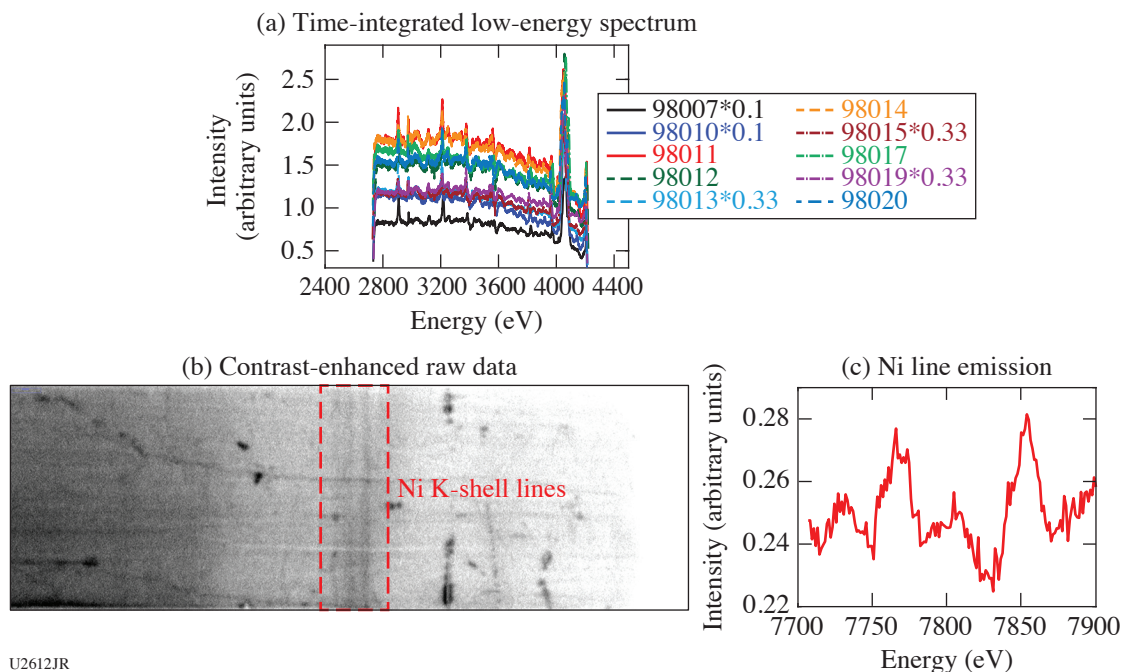(b) Contrast-enhanced raw data

(c) Ni line emission

U2612JR

Figure 13

The performance of the Ni-lined capsule backlighters was very promising for a first experiment with this design. (a) The emission in the spectral range of the Ar K shell is flat continuum. The line emission in (a) is likely the result of mid-Z elements in the glue used to attach the capsules to the stalk. (b) The Ni line emission acts as a second diagnostic probe from a single source with three lines apparent. (c) The line structure shows a relatively bright, high-energy line with two progressively weaker lower-energy lines.

Colliding Megagauss Plasma Jets Experiment

Principal Investigators: E. Liang (Rice University) and L. Gao and H. Ji (Princeton University)

An important question in the study of shock waves, in both astrophysical and laboratory plasmas, is the role of the heat flux carried by electron thermal conduction. When the electron thermal conductivity is high, the conduction front runs ahead of the shock, carries energy upstream, and lowers the post-shock electron temperature. When the electron thermal conductivity is low, the post-shock electrons and ions have roughly the same temperature. Therefore, the shock structure and evolution depend strongly on the electron thermal conductivity. In magnetized shocks, the magnetic field can strongly influence the electron transport. Even if the magnetic field is dynamically unimportant $(B^2 \ll \rho v^2)$, it can still inhibit electron thermal conductivity across field lines, thereby influencing the structure and evolution of the shock. When the electron gyroradius becomes smaller than the Coulomb mean free path, thermal conduction perpendicular to the field lines becomes inhibited, even when the Coulomb mean free path is large, while thermal conduction along the field lines remains uninhibited. In such cases electron thermal conduction can become highly anisotropic, and the structure and evolution of the shock depend strongly on the orientation and strength of the local magnetic field. Our goal is therefore to develop laboratory platforms to systematically study strongly magnetized shocks in controllable settings.

In a series of OMEGA laser experiments in 2016 and 2017,[41,42] we demonstrated that a hollow ring configuration of 20 OMEGA beams irradiating a flat disk can create narrowly collimated megagauss (MG) plasma jets. In such strongly magnetized jets, the electron gyroradii can become much smaller than the Coulomb mean free path. Therefore, we expect that electron thermal conduction will become highly anisotropic. When two such jets collide head on, they will create strongly magnetized high-beta shocks, which should provide a unique platform to study the effects of anisotropic electron thermal conduction on shock structure and evolution. Subsequent 3-D *FLASH* simulations show that the collision of two MG plasma jets, each created by 20 OMEGA beams in a hollow ring pattern, will indeed launch two expanding shocks whose structure and evolution strongly depend on the local magnetic-field geometry and electron thermal conductivity. We were awarded one OMEGA shot date in 2020 and one joint shot date in 2021 to carry out such colliding-jet experiments. At the writing of this report, we just completed our 2020 experiment but the data have not yet been analyzed. Preliminary XRFC images show, however, that expanding shocks were indeed created. We are cautiously optimistic that the data from our 2020 colliding-jets experiment will shed new light on this important question.

Figure 14 depicts the colliding-jet experimental setup. Twenty OMEGA beams from each hemisphere irradiate a flat CH target with a hollow ring pattern of 800-μm radius and 6.4-mm target separation. The Thomson-scattering diagnostic is used to measure the density, electron and ion temperatures, and flow velocity at target chamber center (TCC) and 150 μm below TCC. Protons from a D^{3}He fusion capsule are used to map out the magnetic-field geometry and amplitude. In addition, XRFC is used to capture time-lapse x-ray images of the entire domain. Figure 15 shows 3-D *FLASH* simulation results of this experiment at 4 ns, based on Spitzer thermal conductivity, plus lineout plots along the jet axis. Both the expanding electron conduction fronts and shock fronts are visible, with the conduction front running ahead of the shocks. These predictions will be confronted with our 2020
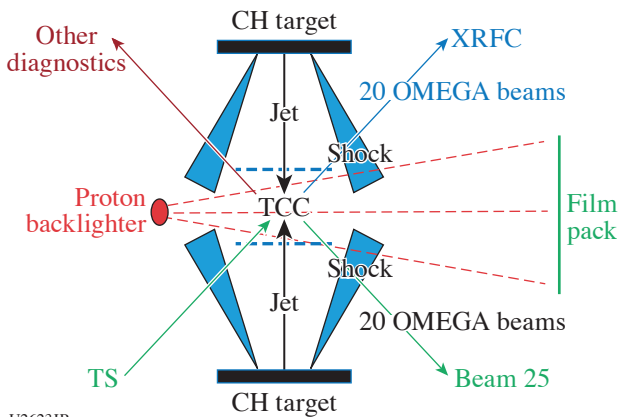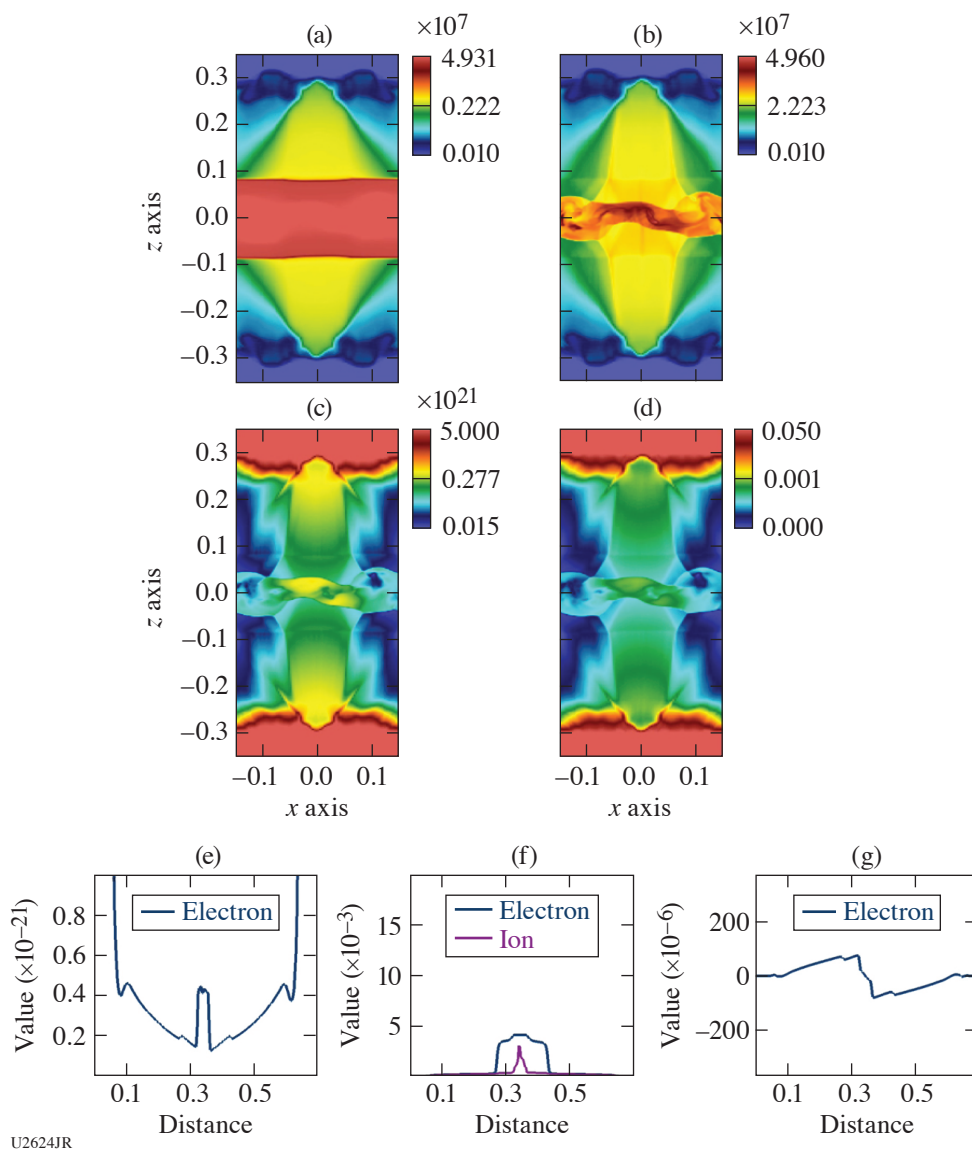

Figure 14
Setup of the colliding MG jets experiment using 40 OMEGA beams.

U2623JR

U2624JR

Figure 15

Three-dimensional *FLASH* simulated profiles of (a) shocked electron temperature, (b) ion temperature, (c) electron density, and (d) ion density at 4 ns. The line plots are profiles along the jet axis of (e) density, (f) electron (blue) and ion (purple) temperatures, and (g) axial velocity at 4 ns.

experimental data. We anticipate the analyses of our 2020 data to be completed in early 2021. This will give us ample time to finalize and refine the design of the follow-on experiment with more-advanced diagnostics, currently scheduled for August 2021.

This material is based on work supported by the Department of Energy National Nuclear Security Administration under Award Number DE-NA0003942.

A Laboratory Photoionized Plasma Experiment on OMEGA EP
Principal Investigator: R. C. Mancini (University of Nevada, Reno)
Co-investigators: R. Heeter and D. Liedahl (LLNL) and S. P. Regan (LLE)

Basic science experiments on high-energy-density (HED) physics on OMEGA EP provide a unique opportunity to create states of matter at extreme conditions of temperature, density, and radiation flux in the laboratory relevant to astrophysics. The focus

of this project is to study the fundamental heating, atomic, and radiation physics properties of plasmas driven by a broadband intense flux of x rays, i.e., photoionized plasmas. Most laboratory work performed to date on HED laboratory plasmas pertains to collisional plasmas, i.e., those where electron collisional processes play a dominant role in the plasma ionization and atomic physics. Relatively little attention has been paid, however, to studying and understanding the basic properties of laboratory photoionized plasmas where both photoionization and photoexcitation, driven by a broadband x-ray flux, become dominant. These plasmas are important for understanding a myriad of astrophysical sources including x-ray binaries, active galactic nuclei, and the accretion disks formed in the vicinity of black holes. The quantitative information that we obtain from these objects is mainly based on the analysis of spectroscopic observations made by orbiting telescopes such as Chandra and XMM-Newton.

We have established a new experimental platform for OMEGA EP that uses a plastic-tamped silicon sample driven by the 30-ns-duration, broadband x-ray flux produced by the "Gatling-gun" radiation source. This source is comprised of three copper hohlraums that are sequentially driven by three OMEGA EP beams, each one delivering 4 kJ of UV energy in a 10-ns square pulse shape. Each copper hohlraum has a length of 2.8 mm and an inner diameter of 1.4 mm and is filled with TPX foam. The laser beams sequentially illuminate one hohlraum at a time, thereby producing an x-ray flux characteristic of 90-eV radiation temperature for a time period of 30 ns. The relatively long duration of the Gatling-gun radiation source is critical to producing an x-ray radiation-driven plasma in photoionization equilibrium.

The silicon sample has a diameter of 2 mm and is placed 7 mm from the source. It has an initial thickness of 0.2 or 0.4 μm and is coated on both sides with submicron-thick, 2.5-mm-diam layers of parylene plastic. Heated by the x-ray flux, the silicon sample expands and ionizes into the L-shell range of silicon ions, i.e., neon- to lithium-like ions, thereby producing a photoionized plasma in steady state with an atom number density of a few times 10^{18} atoms/cm^3 and a relatively uniform spatial distribution.

The spatial extension of the blow-off TPX/copper plasma from the copper hohlraums is monitored with the 4ω probe laser to ensure that it does not reach the silicon sample. The silicon photoionized plasma is probed with L-shell self-emission spectra recorded with a grating spectrometer and K-shell line absorption spectra recorded with a KAP crystal streaked spectrometer. The latter is afforded by a 1-ns-duration, separate titanium backlight source driven by the fourth laser beam of OMEGA EP. This laser beam delivers 1 kJ of UV energy onto a titanium slab target in a 1-ns square pulse shape. The radiative recombination continuum emission photons of the titanium laser-produced plasmas backlight and probe the photoionized plasma via absorption spectroscopy. From this measurement, the charged-state distribution and electron temperature of the plasma can be extracted.

The x-ray flux starts at $t = -15$ ns and lasts until $t = +15$ ns. Figure 16 shows the synthetic spectrally resolved x-ray flux produced by the Gatling-gun source and the measured transmission spectrum of the silicon photoionized plasma at $t = 18$ ns. The data show $n = 1$ to $n = 2$ line transitions in F-, O-, N- and C-like silicon ions as well as $n = 1$ to $n = 3$ in F-like ions. Observations recorded in nominally identical experiments but with the titanium backlighter fired at a later time show a nearly identical absorption spectrum, thereby demonstrating that a plasma in steady state has been produced. The latter is critical to compare with and benchmark the astrophysical modeling codes that are employed in the analysis and interpretation of x-ray astronomy observations.

Platform Development for MagLPI and MagRT on OMEGA EP
Principal Investigators: M. J.-E. Manuel (GA); M. Bailly-Grandvaux, A. Higginson, J. Strehlow, C. McGuffey, and F. N. Beg (University of California, San Diego); R. Lee (University of California, Los Angeles); and C. Samulski and B. Srinivsan (Virginia Polytechnic Institute and State College)

Externally applied magnetic fields have become more common place in HED plasma experiments due in large part to the advancement of pulsed-power technology and new techniques for generating large magnetic fields with laser-driven targets. External magnetic fields applied to inertial fusion experiments can relax the ignition criterion[43] and reduce mix in the hot spot.[44] It is of fundamental interest, then, to understand how external B fields affect laser–plasma[45] and hydrodynamic instabilities in HED plasmas. To that end, the magnetized laser–plasma instability (MagLPI) and the magnetized Rayleigh–Taylor (MagRT) platforms (see Fig. 17) are being developed to answer basic science questions about how B fields affect plasma behavior in laser-driven HED systems.
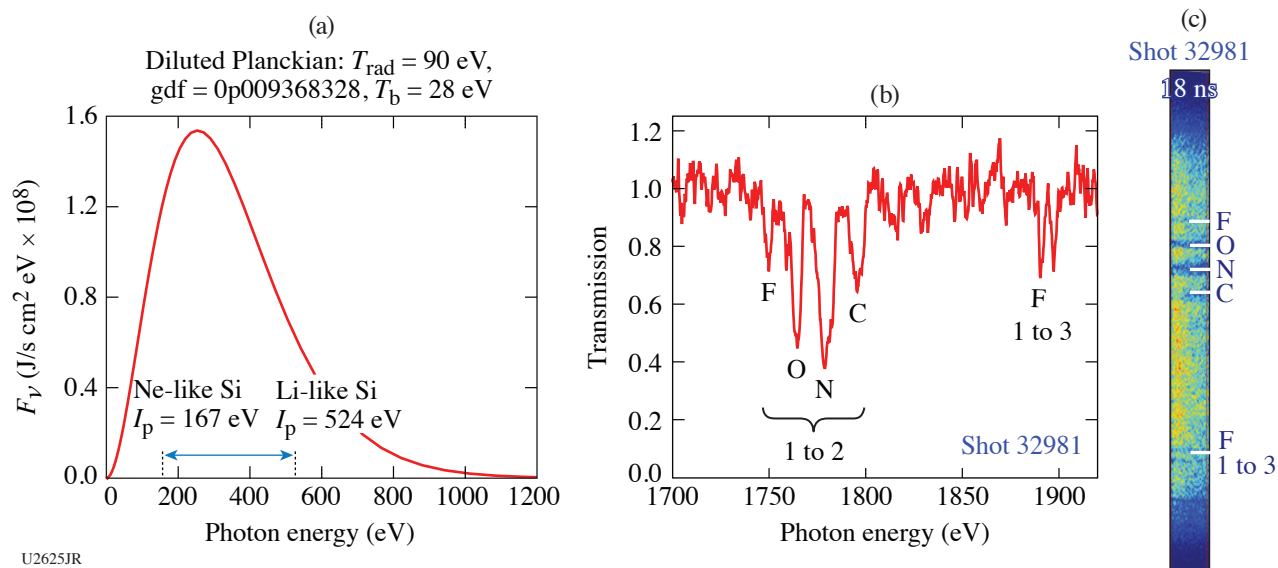
Figure 16
(a) Synthetic spectrally resolved x-ray flux produced by the copper Gatling-gun x-ray source. (b) K-shell transmission spectrum of the silicon photoionized plasma and (c) streaked spectrometer data recorded at $t = 18$ ns on OMEGA EP shot 32981.
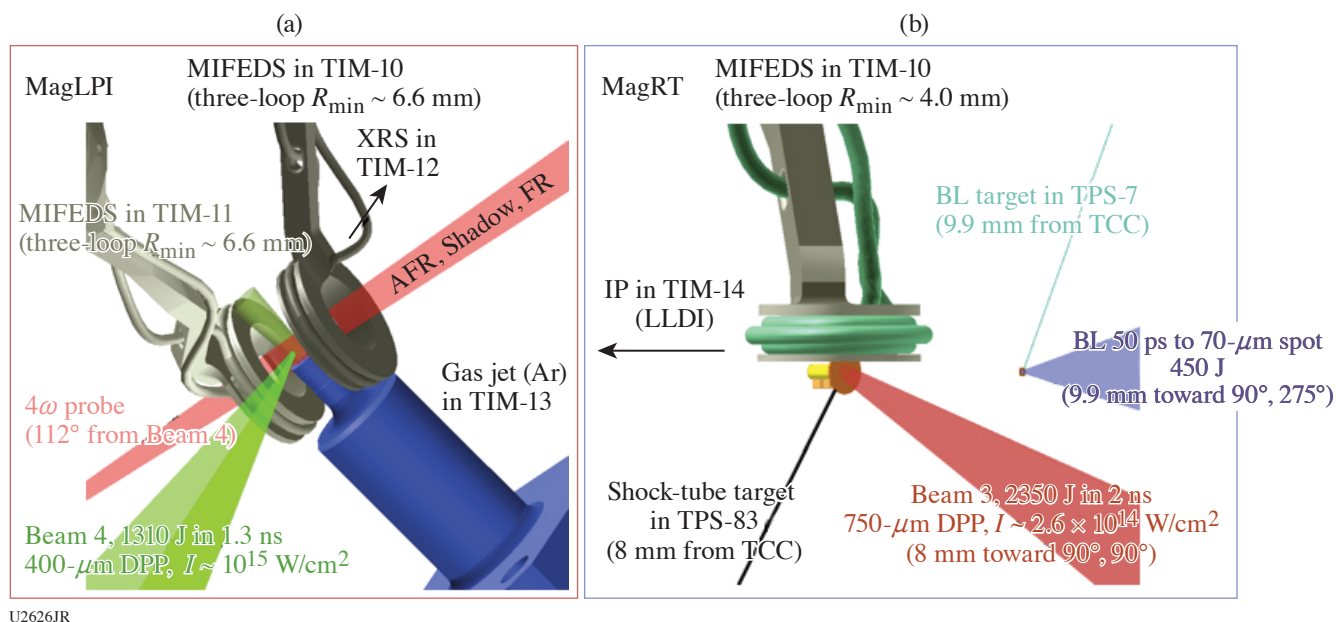

Figure 17
VISRAD configurations for platform development shots executed on 16 July 2020 for the (a) MagLPI and (b) MagRT Campaigns. Backscattered light from LPI's was measured in a laser-driven, magnetized gas jet in the MagLPI Campaign. Blast-wave–driven RT growth in an external B field was imaged with x-ray radiography. Data are presently being analyzed and changes will be coming to both platforms to better study magnetized HED systems.

Charged-Particle Transport and Energy Deposition in Warm Dense Matter With and Without an External Magnetic Field

Principal Investigators: C. McGuffey, M. Bailly-Grandvaux, D. Kawahito, K. Matsuo, K. Bhutwala, J. Kim, M. Dozières, A. Higginson, J. Vaughan, D. Zimmer, and F. N. Beg (University of California, San Diego); D. Mariscal, R. F. Heeter, E. Marley, and J. Emig (LLNL); J. L. Peebles, J. R. Davies, M. S. Wei, P. M. Nilson, W. Theobald, F. J. Marshall, and S. Muller-Fess[*] (LLE); P. Gourdain (Dept. of Physics and Astronomy, University of Rochester); J. Honrubia (Universidad Politécnica de Madrid, Spain); and J. J. Santos (CELIA, University of Bordeaux, France)

[*]Also at GA

In this UCSD-led NLUF project, we investigated the energy deposition in dense matter by two intense-laser–driven particle beams: relativistic electrons and protons. Electron-beam energy deposition was studied in a characterized imploding cylinder with and without an external magnetic field. Understanding the role of the B field is important for advanced fusion schemes such as fast-ignition inertial confinement fusion (FI ICF) and MagLIF. Proton energy deposition was applied to a solid Si foil, turning it into warm dense matter (WDM). Tools to characterize WDM samples are a prerequisite to measurements of equation of state and the benchmarking of proton-stopping codes, which have relevance in ICF capsules and stockpile stewardship.

1. Electron Transport in Magnetized Compressed Matter

The platform used for the study of electron transport is illustrated in Fig. 18. Using a joint OMEGA/OMEGA EP configuration, a plastic cylinder filled with Ti-doped plastic foam is imploded using 36 OMEGA long-pulse lasers;[46] the OMEGA EP short-pulse laser then irradiates one end to produce relativistic electrons that travel into the compressed, magnetized material, where they deposit their energy.[47] Time-resolved spectroscopy and detailed atomic physics codes are used to extract the temperature of the plasma at different levels of magnetization. Electrons reaching and escaping the target are measured via K-shell spectroscopy of tracer foils located on each end of the cylinder. The MIFEDS magnetic-field–generation device delivers 20 T, which, according to our simulations, helps the electrons to efficiently deposit their energy along the compressed channel via magnetic guiding. The experimental observations are compared with particle-in-cell (PIC), hybrid-PIC, and 2-D radiation-hydrodynamic codes to further understand the dynamics.[47]
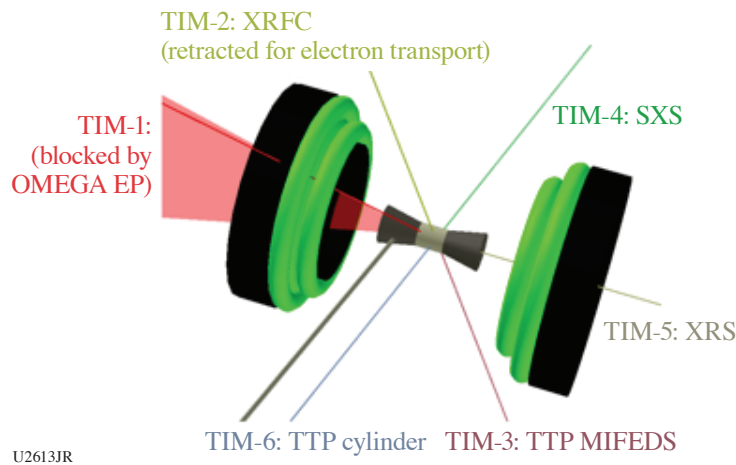

Figure 18
Experimental setup for RelEPlasma-J-20-A.

In Figs. 19(a) and 19(b), we report on recent measurements of the implosion trajectories and stagnation conditions in an implosion-only shot. The results of the implosion history obtained with (a) a fast x-ray framing camera and (b) the time-integrated Ti emission spectra compares very well with our benchmarked 2-D *FLASH* simulation of the implosion. At stagnation, the density is ~10 g/cm^3 and the electron temperature is ~500 eV.

2. Proton Beam Heating and Characterization of Si in Warm Dense Conditions

This portion of the project is focused on proton heating. High-intensity proton beams driven by the 10-ps OMEGA EP laser have been shown to be effective at rapidly heating solid targets into WDM.[48] Now we are developing a reliable temperature-

measurement technique for near-solid, proton-heated samples in the range of 10 to 100 eV. Specifically, an x-ray absorption spectroscopy technique was applied for the first time to a proton-heated sample (Si) using an imaging spectrometer to observe the heating at various times during the heating process.

The dual short-pulse beams were utilized on OMEGA EP with 1100 J in 10 ps for the proton-generating beam and 700 J in 5 ps for the x-ray backlighter, as shown in Fig. 20. The interbeam timing was varied. The wide angular energy distribution of the proton heater beam was measured with radiochromic film stacks (red inset in Fig. 20) on shots with and without the sample to derive a proton source for the modeling effort. Two LLNL multipurpose x-ray spectrometers (MSPEC's) were fielded to obtain reference backlighter spectra and absorption data on all shots.
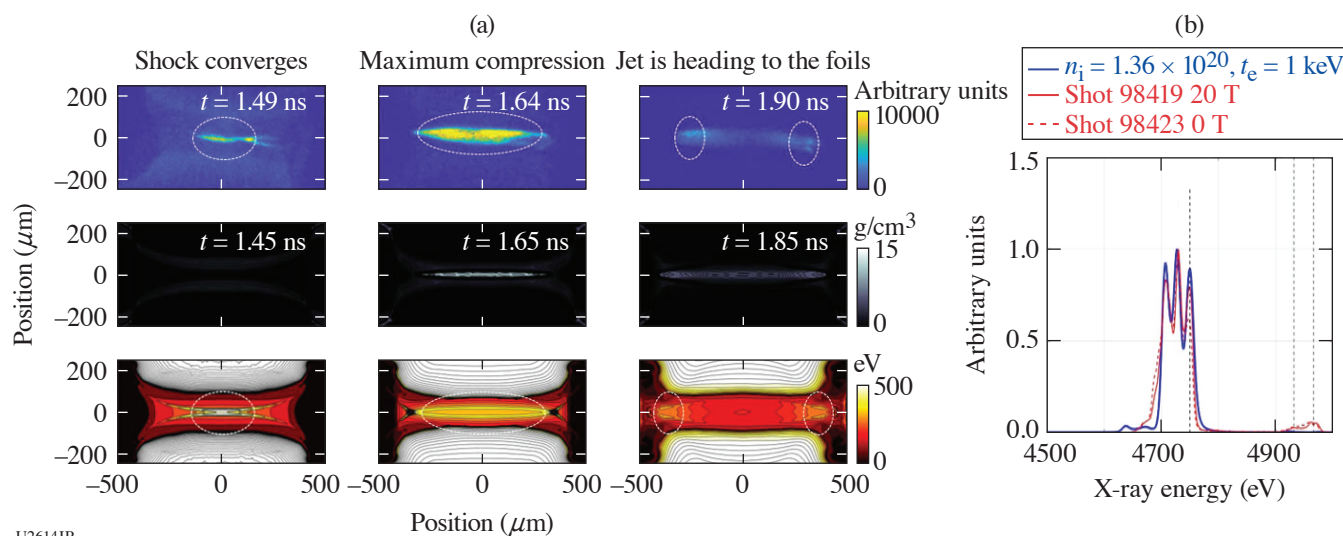
U2614JR

Figure 19

(a) In the first row, snapshots of the implosion (applied $B = 20$ T) measured with an x-ray framing camera and compared with the density (second row) and temperature (third row) histories from 2-D *FLASH* calculations. (b) Titanium spectra measured by a time-integrated x-ray spectrometer for $B = 0$ T and applied $B = 20$ T, compared to *FLYCK* calculations (blue curve) using the density and temperature from the edge of the compressed core as input conditions.
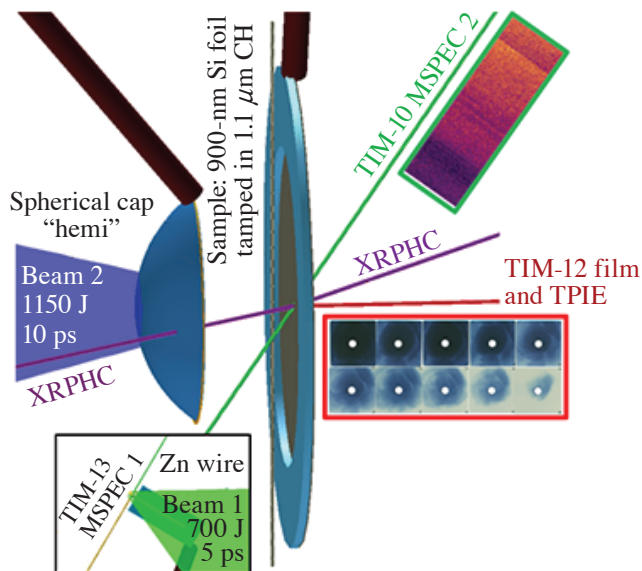
U2627JR

Figure 20

Experimental configuration for the OMEGA EP proton-heated warm dense matter study, ProtonWDM-EP-20A, with radiochromic film and x-ray spectrometer measurements shown in the inset.

High-quality x-ray spectral data, such as the example shown in the green inset in Fig. 20 and the corresponding lineout in Fig. 20, were obtained at five probing delays. Several bound–bound absorption dips below 1850 eV and wide dips above it are, respectively, $n = 1$ to 2 and one to three transitions in ions of Si. Modeling was carried out with 1-D radiation-hydrodynamic simulations and non-LTE (local thermodynamic equilibrium) atomic calculations using codes from Prism Computational Sciences to produce target transmission to compare with the data as shown in Fig. 21. This demonstrates promise for bulk temperature measurements of 10- to 100-eV WDM.

U2632JR
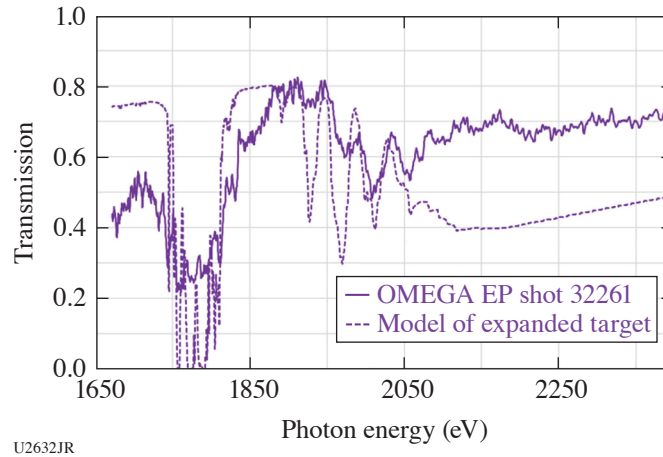
Figure 21

Comparison of modeled and measured transmission of the Si sample at ~86 after Beam 2 irradiated the hemi. The experimental data curve is preliminary pending refined film correction.

Field Measurements from Reconstructions in OMEGA Hohlraum Experiments
Principal Investigators: J. Pearcy, T. Johnson, G. Sutcliffe, A. Birkel, and C. K. Li (Plasma Science and Fusion Center, MIT)

Irradiated by high-power lasers or energetic ions, a high-Z enclosure, i.e., hohlraum, creates an environment filled with a nearly blackbody (Planckian) radiation field. Hohlraum-generated x-ray drive can create extreme plasma conditions and has served as an important platform for studying a wide range of basic and applied HEDP, including laboratory astrophysics, space physics, nuclear physics, and material sciences. In the indirect-drive approach to ICF, a hohlraum is used to generate uniform soft x rays for symmetrically compressing a cryogenic deuterium–tritium (DT) spherical capsule to an extreme state of high temperature and density.

With a typical laser intensity and power irradiating on the hohlraum's inner surface, large-scale, spontaneous electric fields are generated by the electron pressure gradient, and magnetic fields are generated by the noncollinear electron density gradient and temperature gradient (Biermann battery effect). The generation, evolution, and dissipation of such fields are described by the Faraday induction equation along with the generalized Ohm's law. The presence of these electric and magnetic fields has important effects on the plasma transport and dynamics inside the hohlraum.[49] For example, magnetic fields can affect electron thermal transport by changing thermal conductivity, while E fields play an important role in the inhibition of electron heat flux through mechanisms like the return current instability.

To quantitatively study these self-generated spontaneous electric and magnetic fields, advanced proton radiography has been used in producing detailed images of protons being deflected and scattered as they transit through hohlraums as a consequence of sensitivity of charged particles to the fields due to the Lorentz force,

$$\vec{w}_i(\vec{B}, \vec{E}) = \frac{q_i}{m_i c} \int_\ell (\hat{z} \times \vec{B}) dz + \frac{q_i}{\sqrt{2 m_i W_i}} \int_\ell \vec{E} dz,$$

where $\vec{w}_i(\vec{B}, \vec{E})$ is the deflection field. Sponsored by the DOE NNSA NLUF Program, we have recently performed experiments on OMEGA (pProbeHohl-20A). Figure 22(a) shows a schematic of the experimental setup. The backlighter was a D^3He-gas–filled, glass shell capsule with a 420-mm diameter and a 2-mm shell thickness, typically imploded by 30 laser beams. Two types of fusion protons with discrete birth energies of 14.7 and 3.0 MeV were produced in nuclear fusion reactions (D + ^{3}He$\longrightarrow$ α + p and D + D$\longrightarrow$ T + p) ~ 80 ps (the nuclear burn duration). As they transited the hohlraum, the backlighting protons were either deflected by the fields or scattered in the plasma (or wall) and were recorded by CR-39 track detectors.[50] The timing of the proton sampling (i.e., the time when backlighting protons start to pass through the subject target) was adjustable. Figure 22(b) shows a radiograph measured with 14.7-MeV protons.

- By using new techniques, we have been able to quantitatively reconstruct electromagnetic-field information inside laser-driven vacuum hohlraums with field strengths of ~3×10^9 V/m and ~0.5 MG.

- We extracted information from a 14.7-MeV image alone by imposing a systematic relationship between the deflections caused by electric fields and magnetic fields; a particularly simple example is $\vec{w}_{tot} = \vec{w}_B + w_E = (1 - f)\vec{w}_{tot} + f\vec{w}_{tot}$.

- We then tested different values for the breakdown "field fraction" f by using the inferred electric and magnetic fields to predict 3-MeV proton images and compared those to our actual data.
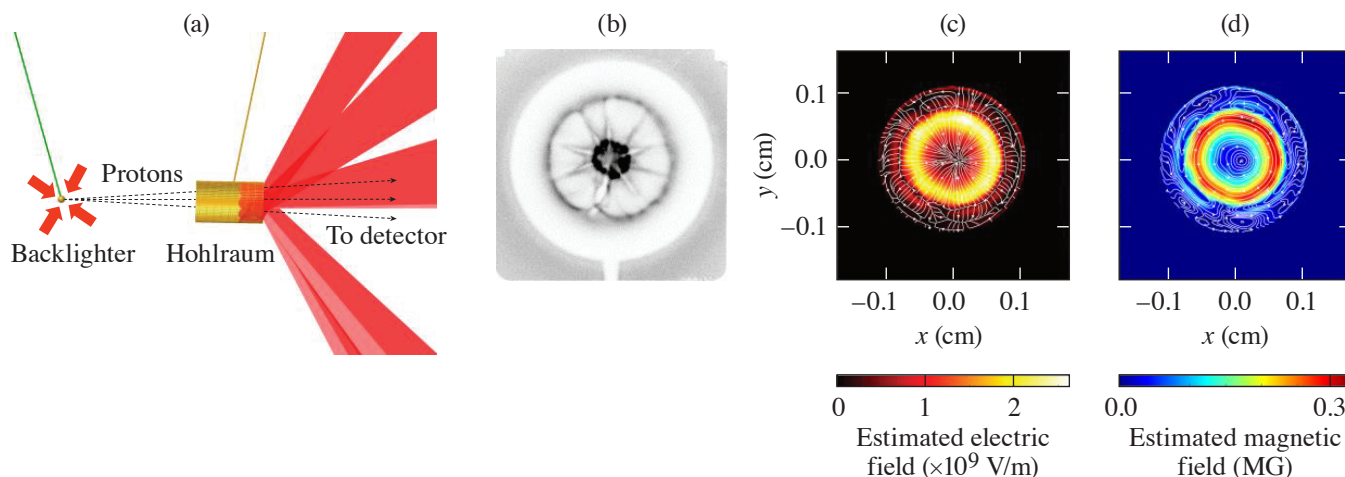
U2615JR

Figure 22
(a) Schematic of the experimental setup; (b) end-on radiographs of a laser-driven "hohlraum" with 15 D^3He protons; (c) reconstructed electric field; and (d) reconstructed magnetic field.

The Dynamics of Strong Magnetic Fields Generated by Relativistic Laser–Plasma Interactions Using OMEGA EP

Principal Investigators: B. K. Russell, P. T. Campbell, C. A. Walsh, G. Fiksel, H. Tang, A. G. R. Thomas, L. Willingale, and K. Krushelnick (University of Michigan); J. P. Chittenden and A. Crilly (Imperial College London, UK); and P. M. Nilson (LLE)

In the interaction of lasers with solid-density targets, large magnetic fields (~MG) can be produced in the expanding plasma plumes. This mechanism has been used to generate experimental geometries relevant to magnetic reconnection, using two plasma

plumes that expand into each other.[51] Previous experiments have been performed using long, moderate-intensity pulses[51] and short, relativistic-intensity pulses.[52] Proton radiography is the standard method used to study these interactions, but it can be very difficult to extract a complete physics picture of the interaction as both magnetic and electric fields are probed, and large errors can occur in calculated field magnitudes without knowledge of the initial proton beam profile.[53] Therefore, we should have a complete knowledge of all parts of the interaction independently to more easily analyze the more-complex interactions.

In FY20 we used two shot days on OMEGA EP to study the fundamental magnetic-field formation mechanisms in short- and long-pulse–generated plasmas. Two 1-ns UV pulses were focused to an intensity of $\sim 10^{14}$ W/cm^2 onto 25-μm-thick films. These pulses had different angles of incidence and were separated such that they would not interact. Protons produced and accelerated by target normal sheath acceleration (TNSA), in the interaction of a 300-J, 1-ps laser pulse with a Cu foil, were used to diagnose the fields produced by the UV lasers in the face-on configuration shown in Fig. 23(a). These probing protons were collected by a stack of radiochromic film (RCF), generating a time series of data on each shot. The time delays between the UV and probe lasers were varied to see the time evolution of the long-pulse magnetic fields. This was performed using Al foils with 1-μm layers of Cu or Au for comparison with data from our previous shot days where we used CH, Cu, and Al foils. A second configuration used a rear-projection probing geometry to study the fields produced by the UV laser at larger angles of incidence and by a second, higher-intensity 500-J, 10-ps IR pulse with an intensity $>10^{18}$ W/cm^2. Si, Al, and CH foils were used for these shots. The probing direction is important to the radiographs produced for the IR pulse because fields produced on the front surface of the target should be imaged as a dot, while back-surface fields should be imaged to a ring. Therefore, information of the front-surface field amplitudes may be lost in the face-on configuration.[54] By probing through the back side of the target, we can reverse this imaging problem and obtain additional information about the front-surface fields.

Figure 23(b) shows the results of our material scan from the long-pulse laser at small angles of incidence. In CH, the radiograph shows a dark ring where protons have been deflected due to azimuthal magnetic fields, similar to the results by Gao *et al.*[55] A notable difference is seen in Al and Cu + Al, where a double-ring structure forms, suggesting the formation of two distinct regions of magnetic field in the plumes. Simulations were performed using the extended-MHD code *GORGON* to understand this discrepancy in the higher-Z targets. At these moderate intensities, magnetic fields are generated by the Biermann battery mechanism, $\partial B / \partial t \propto \nabla T_e \times \nabla n_e$, where ∇T_e and ∇n_e are the gradients in electron temperature and density, repectively.[56] The simulations showed that in the higher-Z targets, two regions with different temperature and density gradients form; therefore, by the Biermann battery, two regions of magnetic field form. This second region, not seen in CH, forms as a result of a change
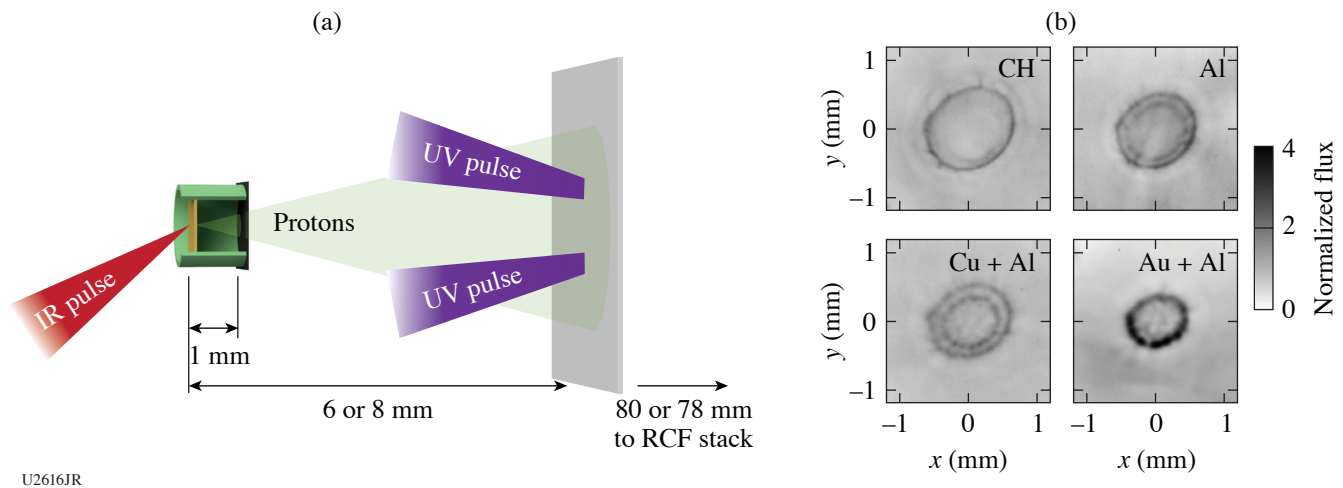

(a) Face-on proton probing configuration used on the first shot day. (b) Proton radiographs of the UV long pulse from FY20 and previous shot days taken for several materials 0.75 ns after the initial time of incidence on the main foil.[57]

U2616JR

Figure 23

in opacity near the edge of the plasma plume from a change in ionization in this region. This charge in opacity will then cause a change in heating in this region from the x rays produced in the hottest regions of the plume. A full analysis of this data was published in 2020.[57]

During the second shot day we took seven shots in the rear-projection probing geometry to study both the magnitude of surface fields produced by a short IR pulse and the structure of UV long-pulse magnetic fields produced at large angles of incidence. Shots taken with the long pulse showed oblong rings with additional rings depending on the material used. These data are currently being analyzed and compared to data taken during the first shot day at large angles of incidence in the face-on probing geometry.

Investigation of Feasibility of the $^{11}B(p,3\alpha)$ Reaction in ICF Settings

Principal Investigators: B. Srinivasan (Virginia Tech); G. Kagan (Imperial College London, UK); M. Gatu Johnson, N. Kabadi, and P. Adrian (MIT); and S. P. Regan, T. R. Joshi, D. Barnak, and R. C. Shah (LLE)

The p11B Campaign aimed to investigate the feasibility of the proton–boron nuclear reaction in inertial fusion settings and to clarify the role of the kinetic effects on x-ray emission from ICF hot spots. A series of exploding-pusher implosions were performed with both nuclear and x-ray diagnostics employed. The nuclear diagnostic relied on CR-39 detecting medium, which is still being processed. The x-ray diagnostic gave good data in both soft (3- to 6-keV) and hard (20- to 30-keV) ranges. In particular, the output from the novel, spatially resolved electron temperature (SR-TE) diagnostic shown in Fig. 24 indicates that the electron temperature profile is rather shallow compared to a reference implosion. Further processing of the x-ray data is ongoing.
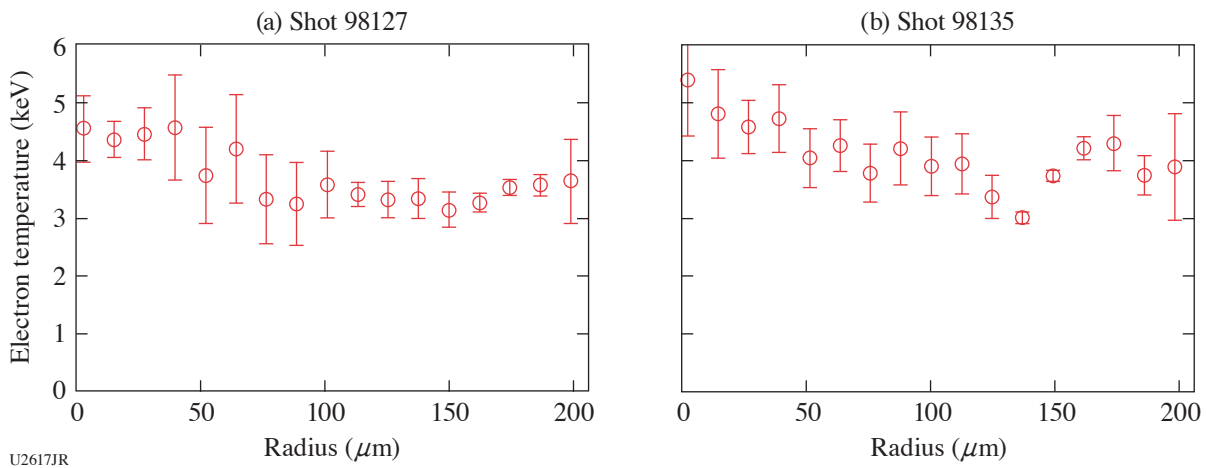

Figure 24
The time-averaged electron temperature obtained with the SR-TE spectrometer for two representative shots 98127 and 98135 as a function of the radial coordinate.

Filamentary Instability Observed in Expanding Laser Ablation Matches PIC Predictions of Electron Weibel Instability
Principal Investigators: G. D. Sutcliffe, T. Johnson, J. Pearcy, B. Lahmann, P. Adrian, N. Kabadi, S. Haque, M. Gatu Johnson, R. D. Petrasso, and C. K. Li, (MIT); B. Pollock and J. Moody (LLNL); and J. Katz (LLE)

In plasmas, gradients in temperature and density are sources of energy available to drive various processes that generate a magnetic field. Chief among magnetic-field–generation mechanisms in plasmas is the Biermann battery, a mechanism that generates large-scale magnetic fields when there are nonparallel density and temperature gradients. This mechanism is both a dominant source of magnetic field in OMEGA laser-driven solid targets (as observed in many references and simulations) and a source of astrophysical seed magnetic fields.[58] Depending on the parameters of the plasma, there is a further variety of processes that contribute to the decay and transport of magnetic fields, including convection, resistive diffusion, and the Hall effect. At long scale length (more precisely, when the magnetic Reynolds number is large), resistive and Hall effects are unimportant and the Biermann battery source term is balanced by convection. This results in a saturated magnetic field scaling $B \propto d_i/L_T$, where d_i is the ion inertial length (set by density) and L_T is the temperature gradient scale length. As the scale length increases, the saturated field strength decreases.

Recent predictions in PIC simulations[59] show that field amplification can proceed instead through the electron Weibel instability in plasmas like that from an OMEGA laser–solid ablation and is important at long scale length L_T/d_i. The structure of the Weibel-amplified magnetic field is necessarily different from the Biermann-generated fields: a small-scale magnetic field is generated around periodic current filaments with wavelengths of the order of the electron inertial length, d_e, much smaller than the macroscopic system size. The simulations predict that instead of the field decreasing with increased L_T/d_i, the field becomes independent of scale length and saturates with $B \propto \sqrt{1/\beta} \approx 1/5$, a larger value than what the Biermann battery could sustain at large L_T/d_i. Indeed, the authors of this summary point out how this finding could change the current model of cosmic magnetic-field generation.

Charged-particle radiographs were collected during MagHohlMultiPBL-19A (a LLNL LBS campaign shared for the primary purpose of "tri-particle" DT^{3}He backlighter development) that showed promising signatures of the Weibel instability: small-scale, filament-structured magnetic fields. BubbleTS-20A was designed to diagnose the plasma as completely as possible for the sake of direct inference of the normalized field scaling quantities β and L_T/d_e and to compare with simulations. A time series of radiographs and Thomson-scattering measurements were collected and are under analysis. An example of the radiographs is shown in Fig. 25, where the filamentary nature of the instability is apparent in the ablated plasma above the foil. From the radiographs, the magnetic field can be inferred through a reconstruction technique that gives both magnitude and wavelength-space
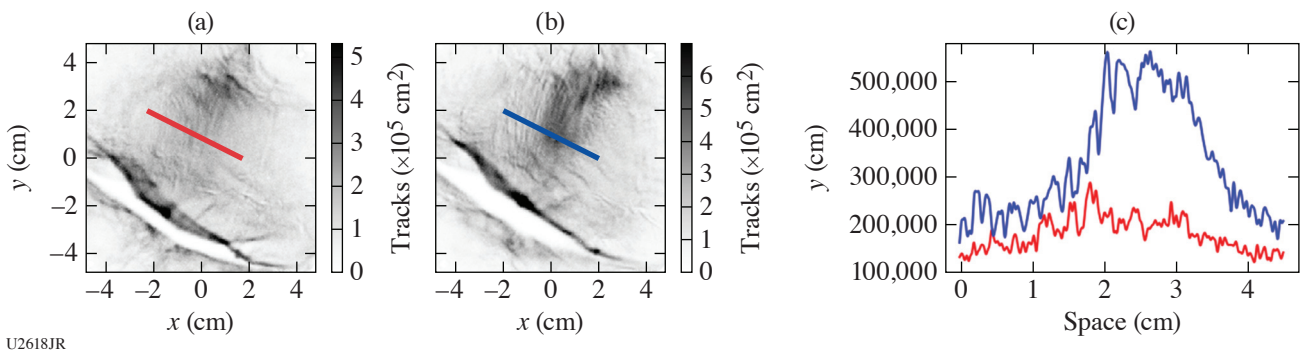

U2618JR

Figure 25
Radiographs collected as part of BubbleTS-20A; D + D proton (~3-MeV) radiographs from shots (a) 96045 and (b) 96046. Here the protons probe the plasma approximately parallel to the foil. (c) Lineouts of the particle flux, with small-scale structure encoding information about the filament-shaped magnetic field generated by (we speculate and seek to prove with further analysis) the electron Weibel instability. The large-scale displacement of particles near the foil is electric-field deflection caused by target charging.

spectral information. These data will ultimately be a test of the PIC predictions and, depending on final results, could shape our understanding of the interplay of magnetic-field–generation mechanisms.

Gas-Filled Hohlraum Hydrodynamic Wall–Gas Interface Stability

Principal Investigators: G. D. Sutcliffe, T. Johnson, J. Pearcy, B. Lahmann, P. Adrian, N. Kabadi, S. Haque, M. Gatu Johnson, R. D. Petrasso, and C. K. Li (MIT); B. Pollock and J. Moody (LLNL); and J. Katz (LLE)

In ICF, "indirect drive" is a configuration where the fusion target capsule is suspended inside a hohlraum. The hohlraum is heated to extremely hot temperatures by laser beams, and the capsule's surface is bathed in x rays from the hot environment. The capsule's surface ablates and the fuel is accelerated inward. Ablated wall material expands into the cavity of the hohlraum. This can prevent laser beam access to the inner sections of the wall and result in large fractions of scattered light. A gas fill can be used to slow the expansion of the wall material. The timing of the laser deposition, and therefore capsule implosion symmetry, depends on the interaction of the ablated wall with the fill gas.[60]

The hydrodynamic stability of the ablated wall and fill gas interface is of interest. Previous gas-filled hohlraum experiments[61] found that the Rayleigh–Taylor instability can explain the chaotic structure in the wall–gas interface. Large density and temperature gradients at this interface could be generating a small-structure, large-amplitude magnetic field that could impact transport in the hohlraum environment. This campaign, HohlraumRT-20A, was designed to systematically look at the growth rate of perturbations imposed in the surface of the wall interface. Gold and CH hohlraums (see Fig. 26) were shot with the laser and probed with proton radiography at staggered times to build a time-resolved understanding of the interface dynamics. Thomson scattering was planned to help connect the experiment with *FLASH* hydrodynamic simulations; however, this diagnostic was dropped after facility issues early in the shot day restricted the number of shots. Analysis of proton radiography data (see Fig. 27) is underway along with supporting *FLASH* simulations.
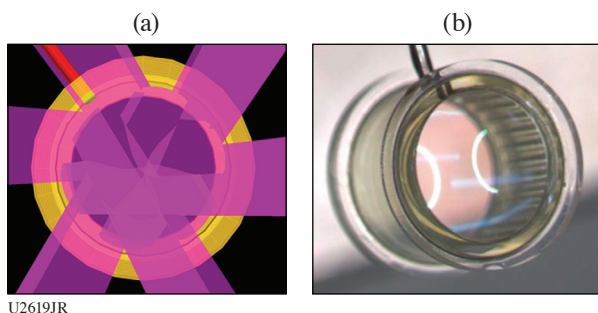
(a) (b)

U2619JR

Figure 26
(a) A VISRAD view of the proton radiography line of sight, along with 6 of the 12 drive beams (6 are on the opposing side); (b) the CH hohlraum. Visible on the far side is the imposed perturbation on the inner surface of the hohlraum. The film holding in the gas fill is also visible as glare.
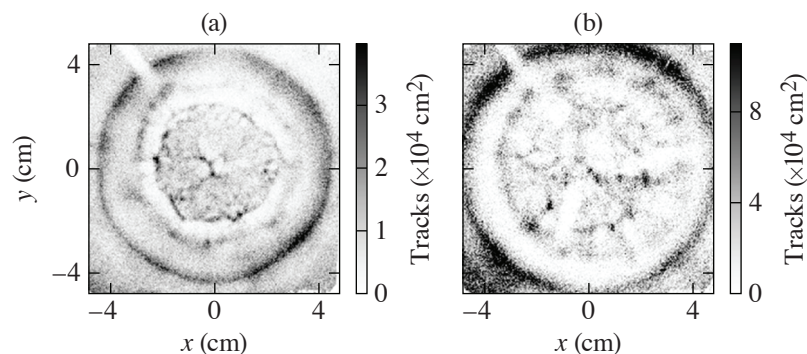

(a) (b)

U2620JR

Figure 27
15-MeV $(D + {}^3He)$ preliminary proton radiographs of (a) the gold hohlraum and (b) the CH hohlraum at late time. Additional etch time is required to improve the quality of the picture, but the wall–gas interface can be seen as a sharp line in the gold hohlraum case. Analysis is underway.

Laser Channeling and Electron Acceleration from High-Intensity Laser Interactions with an Underdense Plasma

Principal Investigators: H. Tang, A. McKelvey, P. T. Campbell, B. K. Russell, Y. Ma, A. G. R. Thomas, and L. Willingale (University of Michigan); H. Chen and F. Albert (LLNL); J. L. Shaw and P. M. Nilson (LLE); and A. V. Arefiev (University of California, San Diego)

High-energy electron beams have numerous applications, including producing highly directional x-ray and gamma-ray radiation.[62,63] This work focuses on the electron acceleration from the interaction of a relativistically intense laser pulse propagating in an underdense plasma. Previous research has used analytical and numerical methods to understand the mechanism of the energy exchange between particles and laser.[64,65] If a laser pulse is intense enough, the electric field can oscillate the electrons at speeds approaching the speed of light, and an electron can be accelerated directly by the laser field and will have momentum gain twice in a laser cycle. But the energy gain is limited by dephasing with laser the pulse.[64,65] Within an underdense plasma, however, global electromagnetic fields can be present. Quasi-static transverse electric fields, caused by the ponderomotive force inducing charge separation between the expelled electrons and the ion channel, and a longitudinal electric field, located near the opening of the channel, become established. These comparatively weak electric fields reduce the electron dephasing and make the transverse velocity antiparallel to the laser electric field, leading to a time extension for the electrons to be accelerated by the laser. A localized azimuthal magnetic field inside the channel is generated by the current flux and can also contribute to energy enhancement by confining the boundaries of the transverse electron motion.

Continuing from previous work that investigated laser channeling[66] and electron heating,[67,68] this project aims to experimentally explore the ideal conditions for generating high-energy electron beams and to observe the channeling dynamics. A picosecond-duration laser pulse was focused onto a millimeter-scale underdense plasma produced by a helium gas nozzle. Plasma densities and laser parameters like pulse duration, energy, and f number were varied to investigate the optimal conditions for electron energy gain. The channel dynamics were observed using proton radiography with RCF stacks.

Figure 28 shows the raw RCF data from a shot using a 111-J, 1-ps laser pulse and plasma density of 0.007 n_c, where n_c is the critical density. For a proton transit time of 117 ps, a time shortly after the main pulse arrives at the gas jet, a channel from the left side to the center of the plasma is clearly observed with a radius of 4.5 μm and a length of 202.7 μm in the interaction plane. The main channel then splits into three branches/filaments and a close-up shows the break-up region. At later times, the "prefocus" filament bundle (left side) grows, surrounding the central channel, and the filamentation structures expand to a larger area on the right side.
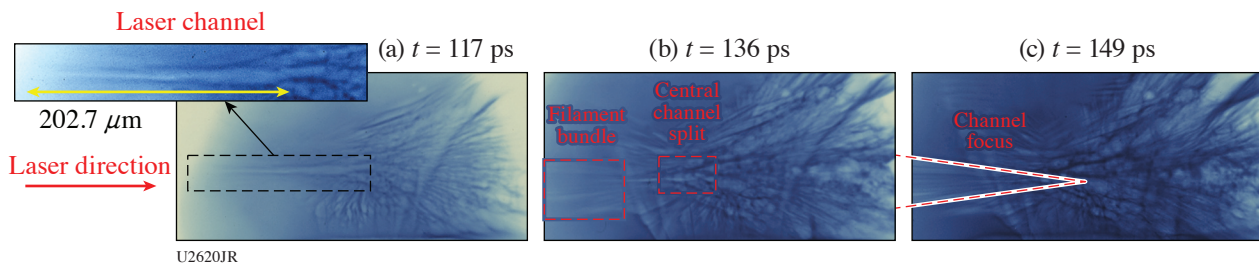

Figure 28
The raw RCF images showing the laser channel and filamentation at t = 117 ps, 136 ps, and 149 ps, where t is the proton transit time from source.

Figure 29 demonstrates the electron energy spectra measured by (a) an on-axis (labeled "head-on") EPPS (electron–positron proton spectrometer) and (b) a transverse (labeled "side-on") EPPS. The blue curves are the background signal obtained from shots with no plasma and are generated by the proton probe–foil interaction. The overlap of the background with other curves in the side-on spectra implies that the majority of the high-energy electrons energized by the main interaction were directed toward the on-axis EPPS. Shots were taken using the square near-field beam profile (approximately equivalent to an f/2 focusing geometry) and a 4-mm-wide nozzle or using an f/2 or f/5 circularly apodized beam and a 2-mm-wide nozzle. The highest electron energy of 70 MeV was achieved using an f/5 circular apodizer, beam energy of 111 J, and plasma density of 0.007 n_c. The mean electron
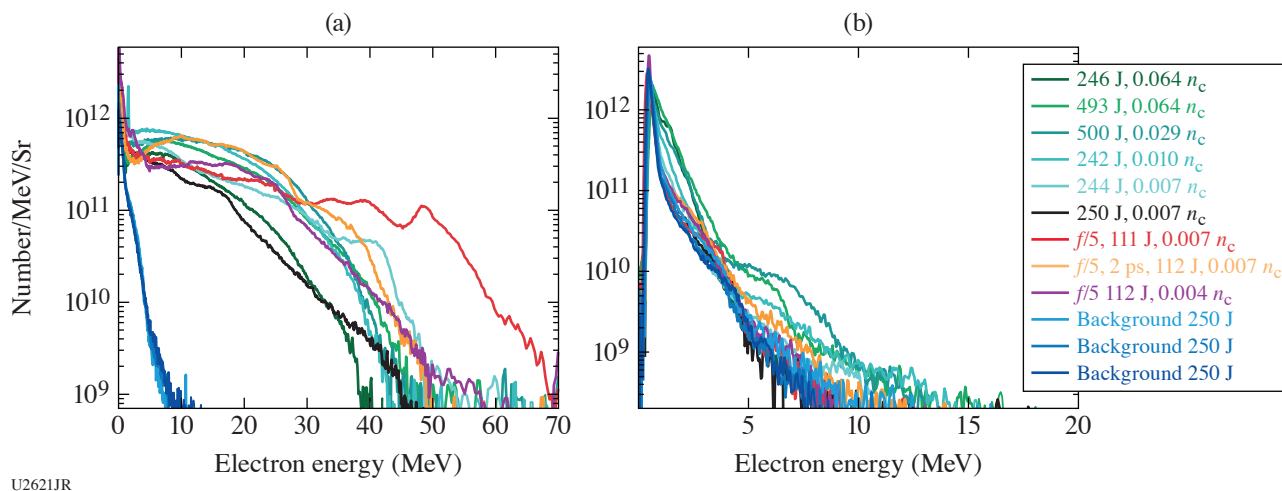
(a)   (b)

U2621JR

Figure 29
The electron energy spectra from (a) an on-axis (head-on) and (b) a side-on EPPS.

energies of nine effective shots vary from 10 MeV to 16 MeV. The low plasma density, low laser energy, and large f number are beneficial to improving the electron energy and number of the accelerated electrons, likely due to improved channel stability.

Quantifying Turbulent Rayleigh–Taylor Mixing with X-Ray Phase Contrast Imaging

Principal Investigators: W. Theobald (LLE); A. Casner, V. Bouffetier, L. Ceurvorst, and F. Barbato (CELIA, University of Bordeaux, France); G. Rigon and M. Koenig (Ecole Polytechnique, France); L. Antonelli, M. Khan, N. Woolsey (University of York, UK); and R. Scott and K. Glize (Rutherford Appleton Laboratory, UK)

The advent of MJ-class laser facilities such as the National Ignition Facility (NIF) and Laser Mégajoule (LMJ)-PETAL makes it possible to explore states of matter in the laboratory that are relevant for astrophysics and HED plasmas under extreme conditions of pressure. For the case of high-Mach-number turbulent flows, NIF and LMJ-PETAL are unique energy drivers because targets are accelerated over larger areas and longer time periods than previously achieved on any other laser facilities. This enables hydrodynamic instabilities, such as the Rayleigh–Taylor instability (RTI) or the Kelvin–Helmholtz instability, to be driven into their turbulent stage of development. However, even though x-ray imaging diagnostics for hydrodynamic instability experiments have improved over the past two decades, further developments are still needed to elevate our understanding and simulations of turbulent flows in HED plasmas.[69]

The planar RTI platform takes advantage of OMEGA EP short-pulse beams to perform wire point-projection x-ray radiography. The platform was first developed at the LULI2000 laser facility in France[70,71] and then successfully transferred to OMEGA EP (TurboHEDP-EP-19A) using classical point-projection x-ray radiography. Here we report on the efforts to apply the recently commissioned x-ray phase-contrast imaging (XPCI) technique,[72] developed by a collaboration of scientists from LLE, the University of York, RAL, and CELIA, to the planar RTI platform. This novel x-ray imager in HED physics could provide electron density gradients as well as additional simultaneous information such as attenuation. Based on the previous results acquired in the TurboHEDP-EP-19A and XPCI-EP-19A experiments, which were performed in 2019 on OMEGA EP, we merged both platforms in order to optimize the configuration and improve the spatial resolution and contrast. A long-pulse UV driver laser impinges onto a plastic ablator foil and generates a shock wave that propagates into a shock tube containing a preheat shield that protects a modulated CHBr foil (5% atomic fraction) that is in contact with a formaldehyde foam ($C_{15}H_{12}O_4$) cylinder. RTI is triggered during the deceleration phase with the modulated surface embedded within the low-density foam. At a time delay of up

to tens of nanoseconds, a high-intensity, short-pulse beam is fired onto the tip of a wire target to provide a point-projection x-ray source, emitting predominantly resonance line emission, and to acquire snapshots of RTI during the highly nonlinear phases. The modulated package (monomode or multimode) decelerates into the lighter foam medium.

It is important to transfer the RTI platform to larger HED facilities such as to drive the modulated CH/foam targets at higher laser energies and with better beam quality. Figure 30(a) shows the VISRAD model of the experiment. Two alternating UV ($\lambda =$ 0.35-μm) drive laser beams (B3, B4) provided an energy of up to 2150 J/beam in a 2-ns square pulse and were focused on the CH ablator mounted onto the shock tube cylinder (1-mm internal diameter, 1 mm in length) filled with a foam with a mass density of 20 mg/cm^3 or 100 mg/cm^3 to trigger RTI growth in the deceleration phase. The UV beams were equipped with SG8-750 distributed phase plates (DPP's) that produced a laser spot with a diameter of 750 μm (1/e value of peak fluence) and a fluence distribution envelope that is well described by a super-Gaussian function with an order of 6.8. The UV laser intensity was 3×10^{14} W/cm^2 per beam at maximum energy. The alternating IR beams (B1 or B2) were focused normal onto the tip of a Ti wire or a Cu wire with an intensity of up to 1×10^{17} W/cm^2 (50 ps, 500 J). The wire was aligned along the axis to TIM-14, which contained a passive image-plate (IP) detector plate in a heavimet-shielded box. The Ti wire backlighter produced a strong emission of between 4.5 and 5.5 keV predominately from the He$_\alpha$ and Ly$_\alpha$ resonance lines, while the Cu wire produced a strong line emission at 8.3 keV from the He$_\alpha$ resonance line. The distance from the backlighter to the CH/foam cylinder was 2.3 cm and the distance from the CH/foam cylinder to the IP detector was 1.4 m, providing a magnification of 60×, which is necessary to observe the phase contrast on the image-plate detector. The technique was first qualified in a shot with a resolution Au grids and a Cu backlighter, demonstrating 15-μm spatial resolution. Subsequent shots with driven targets showed a significant background originating from the main target at maximum laser energy, which overwhelmed the radiograph on the front IP but captured a radiograph on a subsequent IP (back). This is shown in Fig. 30(b). A large Cu washer inside the main target produced significant Cu K$_\alpha$ line emission competing with the backlighter emission and reducing the image contrast. However, a radiograph of the RTI spikes that is visible on the back IP is presumably produced by 10- to 20-keV x rays from the backlighter. Figure 30(c) shows a radiograph of an undriven target, clearly showing the modulated front CHBr plate (in blue), the CH tube containing a 20-mg/cm^3 foam with some defects in it, and the target stalk on the bottom.
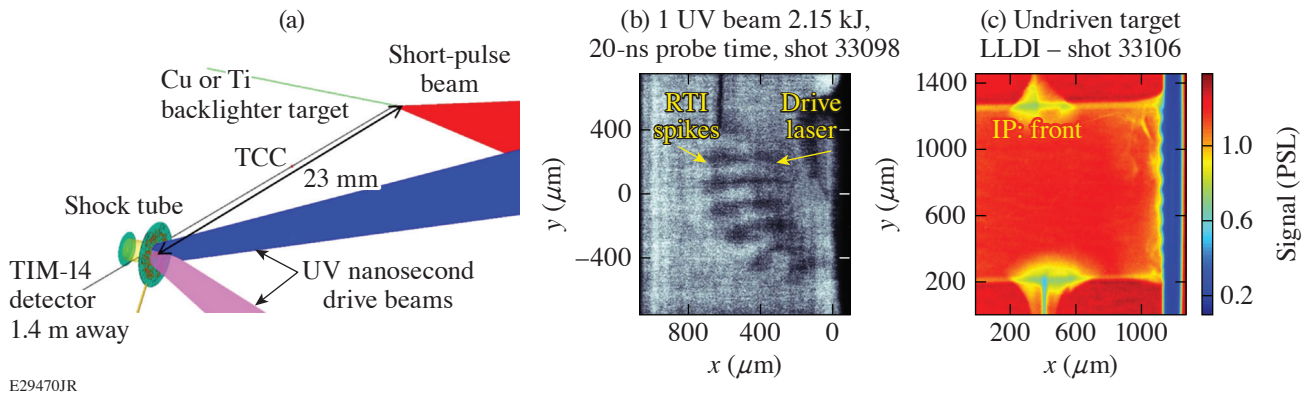

Figure 30
(a) TurboXPCI-EP-20A-aibs VISRAD model and [(b), (c)] experimental data. (b) Radiograph of a single-mode target with initial 100-mg/cm^2 foam density probed at $t = 20$ ns with a Ti wire backlighter. The skew of the shock front due to the non-normal incident drive laser is clearly visible along with the RTI spikes driven into the turbulent regime. (c) Radiograph of an undriven shock tube produced with a Cu wire backlighter. Fine details such as the corrugation of the drive plate (blue region) and fine cracks in the foam material are visible.

In subsequent shots, the background was mitigated by lowering the laser drive intensity producing radiographs on the front IP at various delay times and for two foam densities. The contrast of the radiographs is not, however, at a level to obtain high-quality data. On the other hand, an excellent radiograph of a shock front in a driven CH cylinder was obtained at lower UV drive energy, clearly marking the shock front and phase contrast effects at the target edge (see Fig. 31). Further development, for example by using a time-gated detector, is required to bring this platform to the point where it can be used with high-energy drivers.
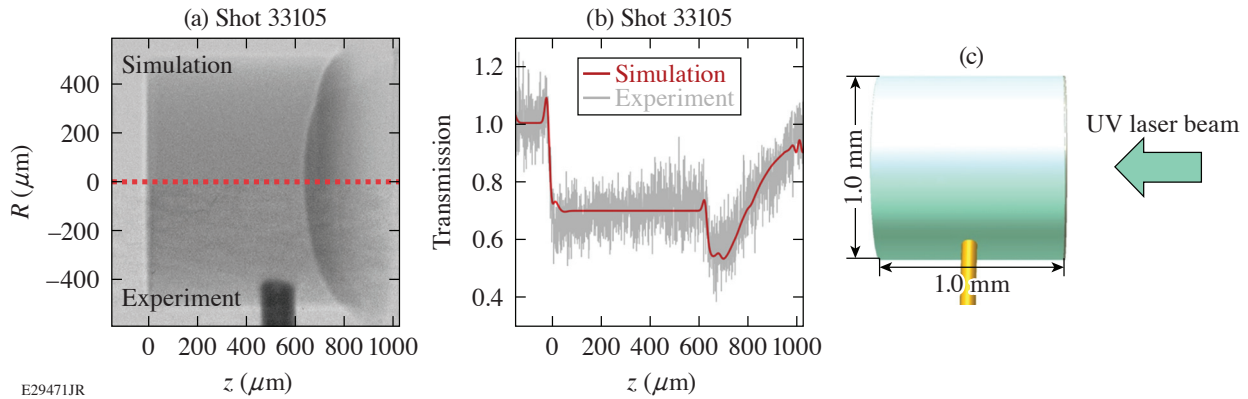
Figure 31
(a) Experimental radiograph (bottom) of a shock wave driven in a solid plastic cylinder compared to a hydro simulation with the code *DUETT*[73] and an XPCI post-processor (top).[72] The signal excursion due to phase contrast on the shock-front interface and the target's back side are observed. (b) Lineout through the central axis of the cylinder. (c) Experimental setup.

Fundamental Astrophysical Processes in Radiative Supersonic MHD Turbulence

Principal Investigators: P. Tzeferacos,*,† E. Hansen, and A. Reyes (Flash Center for Computational Science, Department of Physics and Astronomy, University of Rochester); D. H. Froula and J. Katz (LLE); C. Palmer,‡ A. F. A. Bott,§ T. Campbell, H. Poole, and G. Gregori (Department of Physics, University of Oxford); A. Birkel, C. K. Li, and R. D. Petrasso (Plasma Science Fusion Center, MIT); J. S. Ross and H.-S. Park (LLNL); and D. Lamb (Department of Astronomy and Astrophysics, University of Chicago)
*,†Also, LLE and Department of Physics, University of Oxford
‡Also, Centre for Plasma Physics, School of Mathematics and Physics, Queen's University Belfast
§Also, Department of Astrophysical Sciences, Princeton University

Magnetic fields are ubiquitous in the universe and are salient agents in numerous astrophysical processes;[74] however, their origin is not fully understood. The consensus among cosmologists and astrophysicists is that cosmic magnetic fields are the result of dynamo amplification of tiny seed fields in turbulent magnetized plasmas.[75] The turbulent dynamo mechanism eluded experimental demonstration for decades, while theoretical and numerical studies largely relied on simplified models[76] that steer clear of realistic magnetized compressible turbulence, where strong density fluctuations, shocks, filamentation, and radiative effects complicate the picture and confound the analysis. Only in the last few years have theoretical and numerical efforts begun to tackle highly compressible magnetized turbulence[77,78]—an important step forward, given that most astrophysical systems in the interstellar and intergalactic mediums exhibit signs of high compressibility (i.e., large sonic Mach numbers, M). Supersonic turbulence plays a critical role in determining the star formation rate,[79] the star formation efficiency,[80] and the stellar mass distribution.[81]

Turbulent plasmas also play a fundamental role in the transport and energization of suprathermal particles that make up cosmic rays (CR's). Originally discovered by Hess in 1912 in a series of balloon experiments, today's measurements, based on a combination of balloon, satellite, and ground-based experiments, reveal a power-law spectral energy distribution of CR particles that extends more than ten orders of magnitude[82] up to 10^{20} eV. The origin of these particles puzzled astrophysicists for several decades until Fermi[83,84] showed that charged particles could exchange energy with the plasma by way of scattering off magnetic irregularities. The study of Fermi acceleration in realistic astrophysical turbulence is equally demanding. The kinetic nature of the process and its inherent coupling to the background turbulent plasma complicate modeling efforts. *Ab initio* kinetic simulations using PIC methods are promising,[85,86] but the affordable dynamic range remains limited. Reduced models must therefore invoke simplifications that range from the geometry and properties of the flow, to the transport coefficients of the CR's, to their

interaction with the plasma or lack thereof. While such approaches can inform us on the role and importance of different factors entering the acceleration process, they cannot fully address the integrated problem of Fermi acceleration in magnetized turbulence.

This project aims to demonstrate and characterize for the first time in the laboratory (1) the turbulent dynamo in the radiative, supersonic regime and (2) the acceleration of charged particles via stochastic Fermi in supersonic magnetized turbulence. The experiments exploit the mature turbulent dynamo (TDYNO) experimental platform we developed[87] for the Omega Laser Facility, which demonstrated turbulent dynamo in the laboratory for the first time,[88] and meticulously characterize[89] it in the classical subsonic, nonradiative regime. The TDYNO platform was also used to create an experimental analogue of ultrahigh-energy CR transport in turbulent magnetized plasmas.[90] The experiments build on the expertise we have acquired through our previous experimental campaigns at the Omega Laser Facility and the experience we have gained in designing and interpreting these experiments using validated simulations done with *FLASH*,[91,92] a highly capable radiation MHD code we have developed that is able to simulate a wide range of high-energy-density–physics experiments. The project establishes a basis for laboratory investigations on the nature of the saturated MHD turbulent state in radiative, supersonic turbulence, and poses the basis for understanding the acceleration of charged particles in astrophysical plasmas.

Supersonic magnetized turbulence and the onset of turbulent dynamo were the astrophysical processes we targeted on the first shot day of the TDYNO NLUF experimental campaign. The shot day was carried out on 28 January 2020. The platform deployed is shown in Fig. 32(a) and is similar to the one we fielded on OMEGA for our previous successful TDYNO campaigns. The assembly is comprised of two composite targets and two grids that are connected by a pair of cylindrical shields. The 3-mm-diam composite targets consist of a 10-μm-thick chlorine-doped polystyrene foil (6% Cl) and a 240-μm-thick polystyrene washer. The polystyrene washers were machined to have a 400-μm-diam cylindrical "well" in their centers. The two targets are mounted 8 mm apart and the pair of grids placed between them. The two grids are made of polyimide and are mounted 4 mm apart—each of them 2 mm away from the respective proximate face of the foil target. The grids have a diameter of 3 mm and a thickness of 230 μm and consist of either 300-μm-wide holes and 100-μm wires, or 100-μm-wide holes and 30-μm wires, offset with respect to each other to break the mirror symmetry of the assembly: grid A (red) has a hole in the center while grid B (blue) does not. Rectangular cones on each target shield the diagnostics from the intense x-ray emission produced when a sequence of ten 1-ns-duration laser beams coming from different angles illuminate each target. The two targets are driven for 5 ns, delivering a total of 5 kJ, 2.5 kJ, or 1 kJ on an area defined by the laser SG5 phase plates. The temporal profile of the drive is a "staircase"
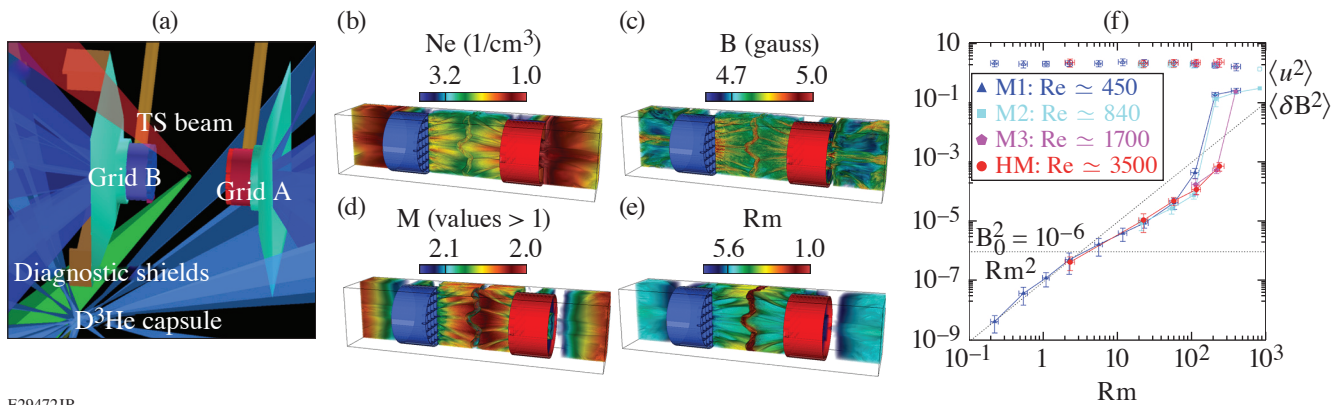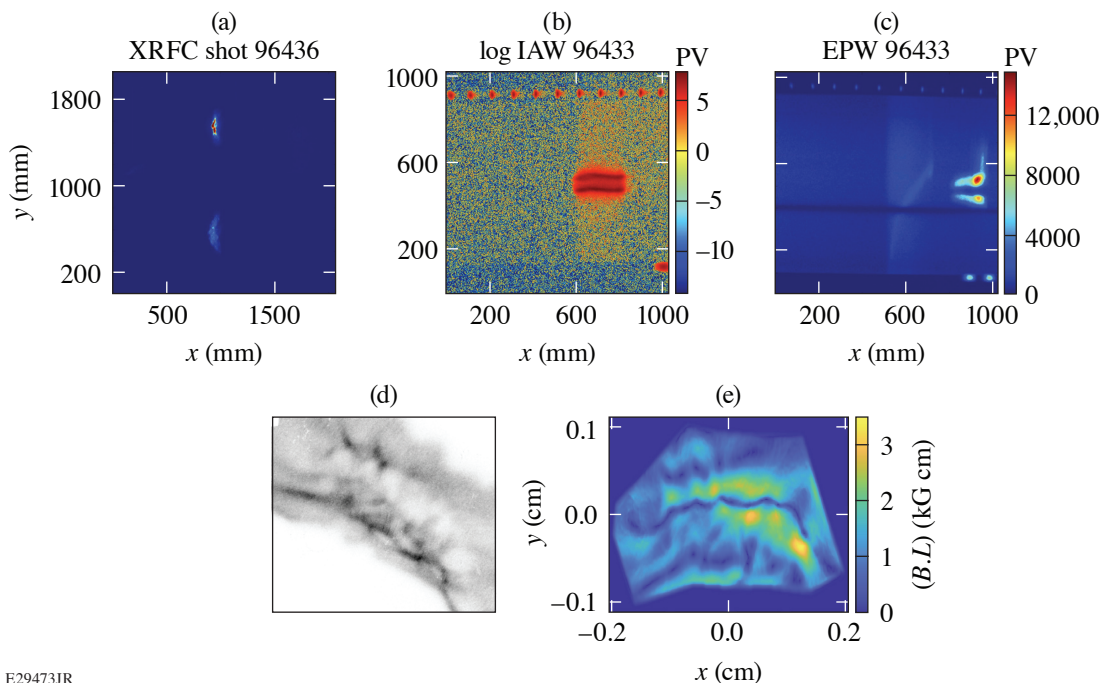

E29472JR

Figure 32

Supersonic turbulent dynamo on OMEGA. (a) *VISRAD* schematic of the supersonic TDYNO platform for OMEGA. (b) *FLASH* simulation of the CHCl platform we will field on OMEGA (electron number density rendering). (c) Magnetic-field strength in the *FLASH* simulation, indicating amplification to hundreds of kG. (d) Mach number of the plasma flows and the turbulent region, showing only values above unity. The turbulent plasma is robustly supersonic. (e) The Rm values in the *FLASH* simulations are above Rm_c in the many hundreds. (f) The mean square induced B field versus Rm from Ref. 93 in the subcritical and supercritical regimes in the subsonic regime. Qualitatively similar behavior is expected for supersonic turbulence.

profile, ramping up the power toward the end of the drive (e.g., for 5 kJ: 500 J/ns for 2 ns, 1000 J/ns for 1 ns, and 1500 J/ns for 2 ns). As shown in the *FLASH* simulation we performed for the platform design, the beams drive a pair of counter-propagating, high magnetic Reynolds number (Rm) plasma flows that carry the seed magnetic fields generated by a Biermann battery. The flows propagate through a pair of grids that destabilize the flow and define the driving scale of the turbulence (*L*). The flows then meet at the center of the chamber to form a hot, turbulent interaction region [Fig. 32(b)] where the magnetic fields are amplified to saturation values [Fig. 32(c)]. The chlorine dopant increases the radiative cooling efficiency of the turbulent plasma. This results in a decrease in the temperature and the sound speed of the plasma, making it supersonic [Fig. 32(d)]. However, our design enabled us to retain large enough temperatures to achieve supercritical Rm for dynamo to operate [Fig. 32(e)].

The primary goals of this shot day were to measure the plasma properties of the supersonic radiative turbulence and the magnetic-field strength during saturation—i.e., at late times of the evolution—as a function of Rm and bracket the critical Rm_c required for the dynamo to operate. We controlled the plasma properties by modifying the laser energy E_{drive} and the driving scale of the turbulence *L* (by using the finer grid). By decreasing E_{drive}, we decreased the turbulent kinetic energy reservoir of the plasma, thereby reducing Rm. Similarly, by reducing *L*, we directly decreased Rm since Rm $\propto$ *L*. The measurements will enable us to (1) demonstrate turbulent dynamo in supersonic, radiative turbulence; (2) experimentally recover the supersonic equivalent of Fig. 32(f), i.e., the Rm dependence of the magnetic field[93] induced by tangling (in the subcritical regime) or dynamo (in the supercritical regime); (3) validate the critical value Rm_c that recent *FLASH* resistive-MHD–driven turbulence simulations place at $Rm_c \sim$ 100 to 170 for supersonic turbulent dynamo;[94] and (4) measure the density, kinetic energy, and magnetic energy power spectra.

The shots yielded a wealth of experimental data: preliminary analysis indicates that we were, in fact, able to generate compressible magnetized turbulence, characterize the plasma state, capture the transition from magnetic tangling to dynamo, and measure the magnetic-field amplification using the suite of diagnostics we previously fielded. More specifically, we used x-ray imaging [Fig. 33(a)] to visualize the formation and evolution of the magnetized turbulence, from which we can reconstruct the density power

Figure 33

Experimental results. (a) X-ray image of supersonic radiative turbulence on OMEGA. (b) IAW 4ω Thomson-scattering signal. (c) EPW 4ω Thomson-scattering signal. (d) Proton radiograph of the magnetized turbulence. (e) Reconstructed path integrated magnetic field[95,96] from the proton radiograph in (d).

spectrum from the x-ray intensity fluctuations and recover temperature maps. Moreover, the 4ω Thomson-scattering diagnostic [Figs. 33(b) and 33(c)] yielded detailed information on the plasma state (ion and electron temperatures, bulk flow velocity, turbulent velocity, and electron density) for different drive/grid combinations. Finally, we employed proton radiography [Fig. 33(d)] on all shots and reconstructed the path-integrated magnetic fields[95,96] [Fig. 33(e)], thereby measuring the magnetic-field amplification and demonstrating weaker fields for smaller values of E_{drive} and L. Despite the complexity of the experimental platform, with the help of LLE personnel we were able to perform 12 shots during our first shot day. The experimental data are currently being analyzed and promise to further our understanding of magnetized astrophysical turbulence in the supersonic regime.

High-Pressure and High-Temperature Polymorphism of a Key Super-Earth Mantle Material: MgO
Principal Investigator: J. Wicks (Johns Hopkins University)

As one of the most important building blocks of the earth and other rocky planets, MgO is a relevant material to characterize at extreme conditions. It serves as a high-pressure analogue for most other diatomic ionic solids, where the B1–B2 transition pressure and mechanism have been studied for decades.[97] The equation of state, phase diagram, and rheology of MgO at the extreme pressures of the B1–B2 transition (300 to 500 GPa) likely play an important role in the mantle convection dynamics of super-Earth interiors.[98]

The high-pressure and high-temperature phase diagram of MgO has been beyond experimental reach until recent years, when groundbreaking research carried out at the Omega Laser Facility identified the B1–B2 transition using streaked optical pyrometry in decaying-shock experiments[99] and then again using x-ray diffraction in laser-driven, ramp-compression experiments.[100] Discrepancies between experimental measurements and theoretically predicted shock Hugoniot(s) (and implied phase diagrams) have been attributed to both kinetics and anharmonicity, exacerbated by the extreme temperatures associated with melting (~10 to15 kK along the Hugoniot).[101]

The goal of this NLUF project is to explore the kinetic barriers to MgO phase transitions along the shock Hugoniot. FY20 marked our inaugural campaign on OMEGA EP, where our primary objective was to carry out temperature measurements of the shock Hugoniot of MgO as a function of shock-propagation direction. Bringing a large team enabled training and experimental support from other lab members from both JHU and Princeton (Fig. 34). This work is part of a continued collaboration between the PI and scientists at LLNL and Princeton, where our common goal is to measure crystal structure and compressibility of minerals under dynamic compression.

In these decaying-shock experiments, 1-ns laser drives are used to drive a strong but unsupported shock wave through the sample assembly. The propagating shock front is monitored using the line-imaging velocimetry (VISAR) and SOP diagnostics, where the properties of quartz windows before and after the MgO served as *in-situ* calibrants[102,103] [Fig. 35(a)]. Discontinuities

in the VISAR and pyrometry records delineate phase changes, enabling one to identify the B2–liquid and the B1–B2 transitions, respectively [Fig. 35(b)].

U2665JR

Figure 34
(a) The science team for this NLUF program's inaugural campaign on OMEGA EP. J. Wicks's laboratory members supported by our colleagues from LLNL, Princeton University, and LLE. (b) Rescheduled COVID-friendly campaign science team.
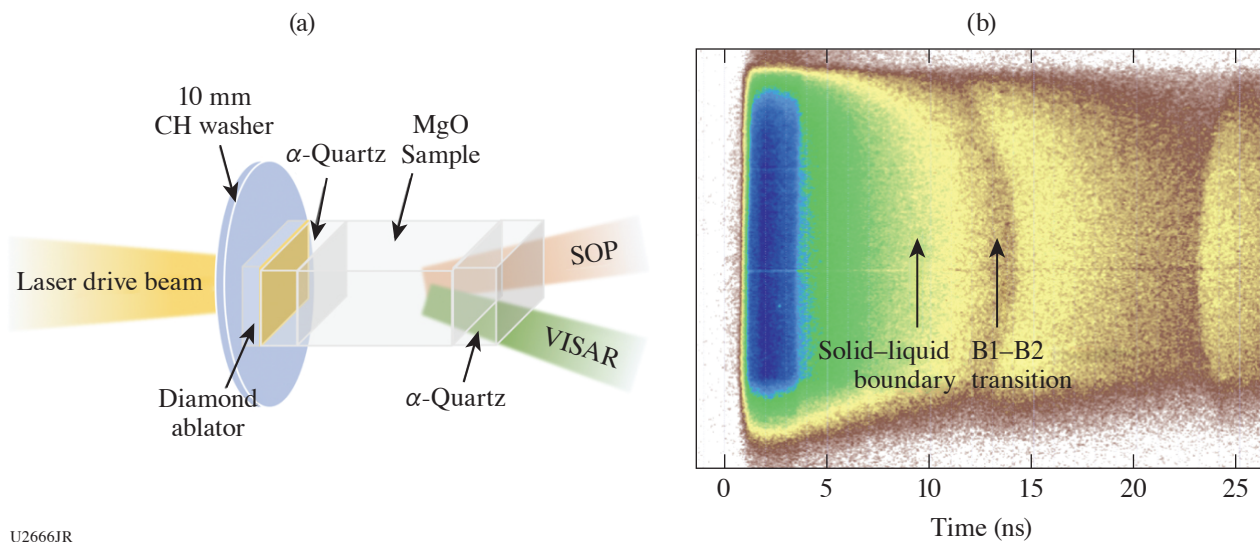
U2666JR

Figure 35
(a) Target setup on OMEGA EP for decaying-shock measurements of single-crystal MgO with quartz reference material. Line VISAR measured the shock velocity and reflectivity of the shock front, while (b) SOP simultaneously measured the thermal emission.

The propagating shock front through both SiO_2 and MgO liquid is a reflective, opaque surface. Below the metallization temperature, the reflected shock is not detectable in VISAR, and pressure is extrapolated as an exponential decay, with end-point pressure constrained by the impedance jump into the quartz window. Decaying-shock measurements of MgO conducted along different crystallographic directions revealed exciting differences in the location and shape of temperature discontinuities along the shock Hugoniot, indicating different transition energy barriers as a function of orientation. Follow-up work using *in-situ* x-ray diffraction will allow us to better understand the temperature trends in the second year of this program.

Another highlight of FY20 was the presentation of this project by former undergraduate researcher J. Gonzalez Quiles at the 2019 Society for Advancement of Chicanos/Hispanics and Native Americans in Science Conference, winning a best poster award. This NLUF grant provided primary support for second-year graduate student Z. Ye (Fig. 34, inset), who spent the following summer studying under Dr. M. Millot (LLNL) through the virtual Livermore Scholars Program. In this internship, she developed and applied optical absorption corrections with the eventual goal to explore transition kinetics effects on optical measurements during dynamic compression experiments.

These results will provide insight into the kinetics effects on the observability of extreme-temperature phase transitions during the time scales of shock compression.

REFERENCES

1. B. Bachmann *et al.*, Phys. Rev. E **101**, 033205 (2020).

2. F. H. Séguin *et al.*, Rev. Sci. Instrum. **74**, 975 (2003).

3. L. X. Benedict *et al.*, Phys. Rev. E **95**, 043202 (2017).

4. J. Daligault, Phys. Plasmas **23**, 032706 (2016).

5. C. R. Scullard *et al.*, Phys. Rev. E **97**, 013205 (2018).

6. D. H. Barnak *et al.*, Phys. Plasmas **24**, 056310 (2017).

7. J. R. Davies *et al.*, Phys. Plasmas **24**, 062701 (2017).

8. E. C. Hansen *et al.*, Plasma Phys. Control. Fusion **60**, 054014 (2018).

9. E. C. Hansen *et al.*, Phys. Plasmas **27**, 062703 (2020).

10. C. A. Walsh *et al.*, Phys. Plasmas **27**, 022103 (2020).

11. R. Florido *et al.*, Phys. Rev. E **80**, 056402 (2009).

12. R. C. Mancini *et al.*, High Energy Density Phys. **9**, 731 (2013).

13. P. Y. Chang *et al.*, Phys. Rev. Lett. **107**, 035006 (2011).

14. M. R. Gomez *et al.*, Phys. Rev. Lett. **113**, 155003 (2014).

15. J. C. Boettger, Phys. Rev. B **67**, 174107 (2003).

16. N. A. Smirnov, J. Phys.: Condens. Matter **29**, 105402 (2017).

17. R. Ahuja, S. Rekhi, and B. Johansson, Phys. Rev. B **63**, 212101 (2001).

18. P. Söderlind, Phys. Rev. B **66**, 176201 (2002).

19. Z.-L. Liu *et al.*, Comput. Mater. Sci. **114**, 72 (2016).

20. L. Dubrovinsky *et al.*, Phys. Rev. Lett. **98**, 045503 (2007).

21. T. Ishikawa *et al.*, Phys. Rev. B **88**, 214110 (2013).

22. A. Dewaele *et al.*, Nat. Commun. **9**, 2913 (2018).

23. R. Briggs *et al.*, Phys. Rev. Lett. **123**, 045701 (2019).

24. S. M. Sharma *et al.*, Phys. Rev. Lett. **123**, 045702 (2019).

25. K. Takemura and A. Dewaele, Phys. Rev. B **78**, 104119 (2008).

26. A. Dewaele, P. Loubeyre, and M. Mezouar, Phys. Rev. B **70**, 094112 (2004).

27. G. Ren *et al.*, Phys. Rev. Lett. **118**, 165001 (2017).

28. W. Riedel *et al.*, High Energy Density Phys. **37**, 100861 (2020).

29. R. A. Treumann, Astron. Astrophys. Rev. **17**, 409 (2009).

30. C. K. Li *et al.*, Phys. Rev. Lett. **123**, 055002 (2019).

31. P. M. Celliers *et al.*, Science **361**, 677 (2018).

32. J. H. Eggert *et al.*, Nat. Phys. **6**, 40 (2010).

33. S. Brygoo *et al.*, J. Appl. Phys. **118**, 195901 (2015).

34. R. Betti *et al.*, Phys. Rev. Lett. **98**, 155001 (2007).

35. S. Zhang *et al.*, Phys. Plasmas **27**, 023111 (2020).

36. Flash Center for Computational Science, University of Chicago, Chicago, IL 60637, Accessed 3 March 2020, http://flash.uchicago.edu/site/.

37. B. E. Robertson *et al.*, Nature **468**, 49 (2010).

38. M. Fraser, R. Soc. Open Sci. **7**, 200467 (2020).

39. R. P. Drake *et al.*, Astrophys. J. **833**, 249 (2016).

40. W. J. Gray *et al.*, Phys. Plasmas **26**, 052901 (2019).

41. L. Gao *et al.*, Astrophys. J. Lett. **873**, L11 (2019).

42. Y. Lu *et al.*, Phys. Plasmas **26**, 022902 (2019).

43. M. M. Basko, A. J. Kemp, and J. Meyer-ter-Vehn, Nucl. Fusion **40**, 59 (2000).

44. B. Srinivasan and X.-Z. Tang, Phys. Plasmas **20**, 056307 (2013).

45. B. J. Winjum, F. S. Tsung, and W. B. Mori, Phys. Rev. E **98**, 043208 (2018).

46. M. Dozières *et al.*, Phys. Plasmas **27**, 023302 (2020).

47. D. Kawahito *et al.*, Phil. Trans. R. Soc. A **379**, 20200052 (2021).

48. C. McGuffey *et al.*, Sci. Rep. **10**, 9415 (2020).

49. P.-E. Masson-Laborde *et al.*, Phys. Rev. E **99**, 053207 (2019).

50. C. K. Li *et al.*, Science **327**, 1231 (2010).

51. P. M. Nilson *et al.*, Phys. Rev. Lett. **97**, 255001 (2006).

52. A. E. Raymond *et al.*, Phys. Rev. E **98**, 043207 (2018).

53. N. L. Kugland *et al.*, Rev. Sci. Instrum. **83**, 101301 (2012).

54. G. Sarri *et al.*, Phys. Rev. Lett. **109**, 205002 (2012).

55. L. Gao *et al.*, Phys. Rev. Lett. **114**, 215003 (2015).

56. L. Biermann and A. Schlüter, Phys. Rev. **82**, 863 (1951).

57. P. T. Campbell *et al.*, Phys. Rev. Lett. **125**, 145001 (2020).

58. R. M. Kulsrud and E. G. Zweibel, Rep. Prog. Phys. **71**, 046901 (2008).

59. K. M. Schoeffler *et al.*, Phys. Plasmas **23**, 056304 (2016).

60. J. D. Lindl *et al.*, Phys. Plasmas **11**, 339 (2004).

61. C. K. Li *et al.*, Phys. Rev. Lett. **108**, 025001 (2012).

62. S. Kneip *et al.*, Phys. Rev. Lett. **100**, 105006 (2008).

63. F. Albert and A. G. R. Thomas, Plasma Phys. Control. Fusion **58**, 103001 (2016).

64. A. P. L. Robinson, A. V. Arefiev, and D. Neely, Phys. Rev. Lett. **111**, 065002 (2013).

65. A. V. Arefiev *et al.*, Phys. Plasmas **23**, 056704 (2016).

66. L. Willingale *et al.*, Phys. Rev. Lett. **106**, 105002 (2011).

67. L. Willingale *et al.*, New J. Phys. **15**, 025023 (2013).

68. A. E. Hussein *et al.*, New J. Phys. **23**, 023031 (2021).

69. A. Casner *et al.,* High Power Laser Sci. Eng. **6**, e44 (2018).

70. E. Brambrink *et al.*, High Power Laser Sci. Eng. **4**, e30 (2016).

71. G. Rigon *et al.*, Phys. Rev. E **100**, 021201 (2019).

72. L. Antonelli *et al.*, Europhys. Lett. **125**, 35002 (2019).

73. S. Atzeni *et al.*, Comput. Phys. Commun. **169**, 153 (2005).

74. E. N. Parker, *Cosmical Magnetic Fields: Their Origin and Their Activity*, The International Series of Monographs on Physics (Clarendon Press, Oxford, 1979).

75. R. M. Kulsrud *et al.*, Astrophys. J. **480**, 481 (1997).

76. A. Brandenburg and Å. Nordlund, Rep. Prog. Phys. **74**, 046901 (2011).

77. C. Federrath *et al.*, Astrophys. J. **797**, L19 (2014).

78. C. Federrath, J. Plasma Phys. **82**, 535820601 (2016).

79. M. R. Krumholz and C. F. McKee, Astrophys. J. **630**, 250 (2005).

80. C. Federrath and R. S. Klessen, Astrophys. J. **763**, 51 (2013).

81. P. Padoan and A. Nordlund, Astrophys. J. **576**, 870 (2002).

82. R. Blandford and D. Eichler, Phys. Rep. **154**, 1 (1987).

83. E. Fermi, Phys. Rev. **75**, 1169 (1949).

84. E. Fermi, *Elementary Particles* (Yale University Press, New Haven, 1951).

85. D. Caprioli and A. Spitkovsky, Astrophys. J. **794**, 46 (2014).

86. L. Comisso and L. Sironi, Phys. Rev. Lett. **121**, 255101 (2018).

87. P. Tzeferacos *et al.*, Phys. Plasmas **24**, 041404 (2017).

88. P. Tzeferacos *et al.*, Nat. Commun. **9**, 591 (2018).

89. A. F. A. Bott *et al.*, Proc. Nat. Acad. Sci. **118**, e2015729118 (2021).

90. L. E. Chen *et al.*, Astrophys. J. **892**, 114 (2020).

91. B. Fryxell *et al.*, Astrophys. J. Suppl. Ser. **131**, 273 (2000).

92. P. Tzeferacos *et al.*, High Energy Density Phys. **17**, 24 (2015).

93. C. Federrath, J. Plasma Phys. **82**, 6 (2016).

94. A. A. Schekochihin *et al.*, New J. Phys. **9**, 300 (2007).

95. C. Graziani *et al.*, Rev. Sci. Instrum. **88**, 123507 (2017).

96. A. F. A. Bott *et al.*, J. Plasma Phys. **83**, 905830614 (2017).

97. Y. Syono, Y. Noguchi, and K. Kusaba, in *Properties of Earth and Planetary Materials at High Pressure and Temperature*, edited by M. H. Manghnani and T. Yagi, Geophysical Monograph Series (AGU, Washington, DC, 1998), Vol. 101, pp. 319–325.

98. S. Karato, Icarus **212**, 14 (2011).

99. R. S. McWilliams *et al.*, Science **338**, 1330 (2012).

100. F. Coppari *et al.*, Nat. Geosci. **6**, 926 (2013).

101. J. Bouchet *et al.*, Phys. Rev. B **99**, 094113 (2019).

102. M. D. Knudson and M. P. Desjarlais, Phys. Rev. B **88**, 184107 (2013).

103. D. G. Hicks *et al.*, Phys. Rev. Lett. **97**, 025502 (2006).